Naval Research Laboratory
Washington, DC 20375-5320

NRL/6362/MR—2021/3

Theory and Modeling of Ultrafast Electron Emission from Nanostructures

DR. KEVIN L. JENSEN

DR. ANDREW R. SHABAEV

DR. MICHAEL OSOFSKY

Materials Physics and Chemistry Section
Materials Science and Technology Division

September 30, 2021

REPORT DOCUMENTATION PAGE

Form Approved
OMB No. 0704-0188

1. REPORT DATE *(DD-MM-YYYY)*	**2. REPORT TYPE**	**3. DATES COVERED** *(From - To)*
30-09-2021	NRL Memorandum Report	April 26, 2021 – September 30, 2021

4. TITLE AND SUBTITLE

Theory and Modeling of Ultrafast Electron Emission from Nanostructures

5a. CONTRACT NUMBER

5b. GRANT NUMBER

5c. PROGRAM ELEMENT NUMBER

6. AUTHOR(S)

Kevin L. Jensen, Andrew Shabaev, and Michael Osofsky

5d. PROJECT NUMBER

5e. TASK NUMBER

5f. WORK UNIT NUMBER
1X48

7. PERFORMING ORGANIZATION NAME(S) AND ADDRESS(ES)

Naval Research Laboratory
4555 Overlook Avenue, SW
Washington, DC 20375-5320

8. PERFORMING ORGANIZATION REPORT NUMBER

NRL/6360/MR--2021/3

9. SPONSORING / MONITORING AGENCY NAME(S) AND ADDRESS(ES)

Naval Research Laboratory
4555 Overlook Avenue, SW
Washington, DC 20375-5320

10. SPONSOR / MONITOR'S ACRONYM(S)

NRL-NISE

11. SPONSOR / MONITOR'S REPORT NUMBER(S)

12. DISTRIBUTION / AVAILABILITY STATEMENT

DISTRIBUTION STATEMENT A: Approved for public release; distribution is unlimited.

13. SUPPLEMENTARY NOTES

14. ABSTRACT

The generation of electron beams is directly dependent upon the physics of the emission process. The prediction of beam properties is essential for the predictive design and development of technologies of critical importance to devices that rely on tunneling and/or vacuum transport, particularly in nano-devices and harsh environments such as pulses drawn from carbon fibers. The present study documents the overall theoretical effort on the tunneling time problem, thermal field emission, and heating effects in microstructures.

15. SUBJECT TERMS

Vacuum nanoelectronics; Electron beam; Electron emission; Thermal-field emission; Tunneling time; Heating; Carbon fiber emitters

16. SECURITY CLASSIFICATION OF:			**17. LIMITATION OF ABSTRACT**	**18. NUMBER OF PAGES**	**19a. NAME OF RESPONSIBLE PERSON**
a. REPORT	**b. ABSTRACT**	**c. THIS PAGE**			Kevin Jensen
U	U	U	U	34	**19b. TELEPHONE NUMBER** *(include area code)* (202) 767-3114

Standard Form 298 (Rev. 8-98)
Prescribed by ANSI Std. Z39.18

This page intentionally left blank.

Contents

1 Abstract

The generation of electron beams, and their subsequent manipulation, is directly dependent upon the physics of the emission process, especially for high brightness beams, but those methods when used in beam simulation presume instantaneous emission using 1D semi-analytic theories applied to static barriers. The prediction of beam properties is essential for the predictive design and development of technologies of critical importance to devices that rely on tunneling and/or vacuum transport, particularly in nano-devices and harsh environments such as pulses drawn from carbon fibers. Emission modeling is used to simulate many DoD technologies: High Power Microwave (HPM) devices, Directed Energy, RF/THz technologies, EW, multi-$e$beam lithography, electron microscopy, radiation hard and/or high temperature electronics, rf and voltage breakdown, micro-discharges, ion propulsion / microthrusters for satellites, space mission electronics. The present study documents the overall theoretical effort on the tunneling time problem, thermal field emission, and heating effects in microstructures.

This page intentionally left blank.

2 Introduction

2.1 Background

The generation of electron beams, and their subsequent manipulation, is directly dependent upon the physics of the emission process, especially for high brightness beams, but those methods when used in beam simulation presume instantaneous emission using 1D semi-analytic theories applied to static barriers. The prediction of beam properties is essential for the predictive design and development of technologies of critical importance to devices that rely on tunneling and/or vacuum transport, particularly in nano-devices and harsh environments such as pulses drawn from carbon fibers. Emission modeling is used to simulate many DoD technologies: High Power Microwave (HPM) devices , Directed Energy, RF/THz technologies, Electronic Warfare, multi-*e*beam lithography, electron microscopy, radiation hard and/or high temperature electronics, rf and voltage breakdown, micro-discharges, ion propulsion / microthrusters for satellites, space mission electronics.

Thermal-field emission electron sources that can meet taxing performance demands, withstand radiation-hard and poor vacuum environments, and enable thermally tolerant electronics will contribute to many emerging technologies [1]. Performance, ruggedness and survivability are stressed. For nanogap devices (*e.g.* nano-vacuum channel transistors (NVCT) and photo-excited structures [2, 3, 4, 5]), a vacuum channel circumvents technological obstacles caused by, first, significant Joule heating in the transport channel and Nottingham heating at the emission site [6], and second, radiation damage to electronic materials. Ballistic transport in a vacuum channel does not generate heat, and realizable vacuums have an enormous breakdown threshold ($\mathcal{E}_{bd} \sim 100$ MV/m). The ratio of the anode-cathode (AK) separation L with the transit time τ replaces the semiconductor saturation velocity $v_s \to L/\tau$ in Johnson's figure-of-merit [7] ($\mathbb{J} = \mathcal{E}_{bd} v_s/2\pi$): for example, nano-vacuum channel transistors (NVCT's) enable $\mathbb{J}_{vac} > 10^3 \times \mathbb{J}_{Si}$ (in contrast, $\mathbb{J}_{GaN} = 15.4 \times \mathbb{J}_{Si}$). Emission into vacuum is by quantum mechanical tunneling through a surface barrier (Φ), but the physics applies equally well to microscopy, MIM and nanodiode structures. Tunneling occurs when the DeBroglie wavelength λ_B of an electron ($-q$) satisfies $q\mathcal{E} \approx \Phi/\lambda_B \sim 9$ GV/m. Nano-dimensioned AK gaps (smaller than mean free path) extend advantages by substantially relaxing vacuum requirements. For nanofiber and nanotubes, heating changes *field* to *thermal-field* emission [8, 9] because of strong temperature gradients and non-linear heat loss factors, making prediction very difficult and undermining characterization of emission properties using conventional steady state models [10, 6]. Dynamic effects of ions approaching surfaces influence breakdown behavior in poor vacuum (Paschen's Law). Not all thermal-field emission is an opportunity: undesirable microprotrusions on metal surfaces contribute to high-field breakdown in high power devices and is described by similar physics.

2.2 Overview

This report describes efforts to create theoretical models of thermal-field emission with position-dependent temperature variation and dynamic processes using methods derived from quantum distribution, transfer matrix (tunneling), thermal-field emission, and heat transport / radiative loss methods, so as to develop computationally rapid algorithms appropriate for beam optics codes treating ultra-fast / ultra-small processes. The models are to address the simulation of ultrashort electron pulses in vacuum for nano-devices and rapidly heated nanotube / fiber emitters that have complex emission barriers and dynamic launch conditions associated with time-dependent and non-uniformly heated surfaces. Nanodevices entail novel tunneling barriers affected by charge in the anode-cathode (AK) gap which leads to "noise" and stochastic processes. Nanofibers have temperature gradients along the fiber that can approach "runaway" conditions. Many time scales are involved: tunneling time, ultrafast field variation, electron relaxation time during transport, heat diffusion times from Joule and Nottingham effects but opposed by radiative heat lost processes, and nanoscale anode-cathode (AK) gap transit times. They depend on current governed by local thermal-field (TF) emission processes [8, 9] past barriers associated with coatings and heterostructures [1], and space charge oscillations. Computationally efficacious models are for, *e.g.*, particle-in-cell and molecular dynamics codes used to describe electron sources with strong TF and temporal variations as part of their normal operation in a manner allowing for treating the consequences of finite tunneling, scattering, and AK gap transit times on the emission process.

Manuscript approved September 29, 2021.

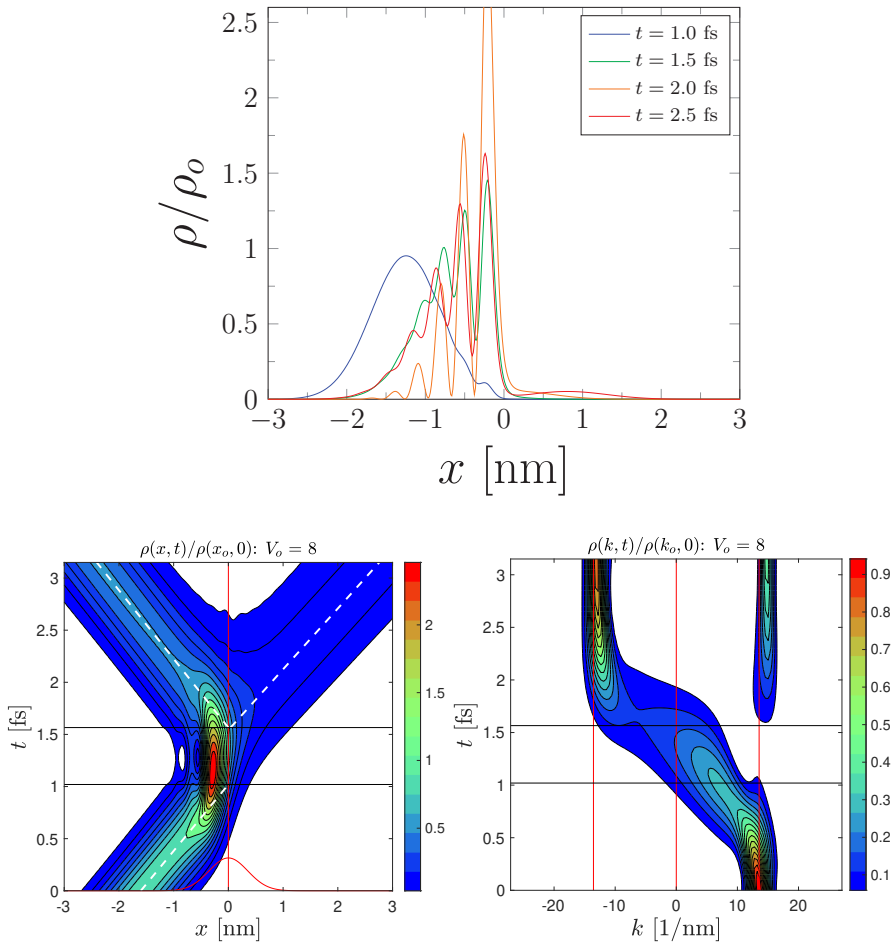

Figure 1: *(top) Density $\rho(x,t)$ evolution of QDF Gaussian wave packet incident on gaussian barrier of height V_o and width λ at different times. Barrier centered at $x = 0$ (left) number density $\rho(x,t)$: dashed lines are trajectories of centers of packets and gap between lines is time delay induced by tunneling / emission. Red curve on bottom is $V(x)$. (right) $\rho(k,t)$ as contour plot: ridge maxima at top give center momenta. After Ref. [15].*

Emission events in simulation codes are commonly treated as instantaneous (applied fields are static) because the relevant time scales of changes are generally long compared to those of emission itself (tunneling, scattering, transit times, radiative processes): simulations of wave packets upon barriers using a quantum distribution function (specifically, the Wigner Distribution Function (WDF)) show that the packets are delayed in time compared to trajectories that follow a ballistic model, as shown in Figure 1. More egregiously, current at the presumptive emission site is treated using only one of the asymptotic current limits associated with *either* field *or* thermal emission, when in fact emission from thermal-field conditions can be orders of magnitude larger [Fig. (1d)], and past barriers that depart from the assumed "image charge potential barrier" of the canonical emission equations. These complications attend nanogaps [11, 12] and short bunches (particularly when from nanotubes and fibers) [10] in particular, for which the static environment / instantaneous emission / field or thermal approximations are ill suited. Recent developments using Schrödinger Equation (SE) [13, 9, 1] and quantum distribution function (QDF) [14, 15] methods provide a basis to formulate thermal-field and time-dependent emission models which allow for the simulation of dynamic processes, *e.g.*, ones that can contribute to breakdown and/or thermal runaway along fibers [6], and offer reasonable models of delays due to over-barrier and tunneling transport.

Relevant time scales are: ultrafast bunches (10 - 1000 fs); scattering in bulk (1 - 100 fs); electron AK gap

transit times [11] (electrons travel 100 nm in 15.1 fs for $\mathcal{E} = 5$ GV/m); and Büttiker-Landauer semiclassical times ($\tau_{sc} \sim \Phi/q\mathcal{E}v_F \approx 0.6$ fs) characterize tunneling delay [Fig. (1c)]. Noise (random emission events), intrinsic emittance (reduces beam brightness), and launch angle (causes gate interception or beam spread) depend on temperature and the local variation of the emission barrier due to coatings and heterostructures [16]. To connect dynamic quantum behavior to trajectory and beam optics, emission models must provide (*i*) the dependence of current density on *local* field and temperature conditions which change along the structure, (*ii*) the resulting field emission velocity distribution from the surface, (*iii*) the mean transverse energy (MTE) at the emission site which is the dominant component of intrinsic emittance, and (*iv*) the launch time of the particle once chosen to be emitted. All manifest as $I(V)$ hysteresis, duty cycle variations, or time-dependent evolution, and so conventional asymptotic steady state derived algorithms in simulation are undermined [16].

Moreover, semiconductor field emission (as from carbon fibers) entails significant heating that can occur along fibers, nanotubes, or high aspect ratio nanowires when driven to large per-tip currents [9, 6], such that existing models cannot anticipate thermal runaway (emitters are commonly current-limited to 1 μA/tip to prevent failure in nanogap devices). Variations in doping and quantum mechanical confinement (discrete energy levels associated with triangular wells depend on doping) change band bending effects at the surface and the presence of oxides alter the tunneling barrier and make the tunneling theory substantially more difficult [13, 1]. Dynamic theoretical emission models must be computationally tractable to be useful to device and beam simulation, in ways that density functional theory (DFT) is emphatically not and Transfer Matrix Approach (TMA) methods for tunneling not very well, as the surface mesh describing just the emitter has millions of elements contributing to total current in a simulation. Proposed theory enables predictive simulations of *ultrafast and ultrasmall emitter* conditions and trajectory mapping by creating parametric and computationally rapid theoretical models vetted by more comprehensive theoretical methods. Relating emission to dynamic processes changes the modeling paradigm significantly. As a consequence, efforts are directed to providing a means to, first, develop emission velocity and launch time models so as to create launch conditions for simulations that account for dynamic changes in the emission barrier due to field variation and emission fluctuation, and second, evaluate self-consistent temperature variation along nanowires caused by the coupled general thermal-field current (GTF) [8], consider non-standard barrier models vetted using transfer matrix approach (TMA) methods, and accounting for launch delay associated with passage over and through barriers.

3 Tunneling Delay

A method to model how long an electron spends tunneling through a barrier is developed. It has taken on increasing importance for nanogap devices [3, 17, 18] such as nanoantennas for which field emission occurs across an anode-cathode (AK) gap of 50 nm [4] down to 8 nm [5] (where the anode-cathode transit time [19] is on the order of femtoseconds). Hartman [20] (see also McColl [21]) found that the transmission time for a metal-insulator-metal (MIM) thin film was given by the group delay $\tau_g = \hbar/\sqrt{\mu\Phi}$ in the limit of large barrier width, where μ is the Fermi level and Φ is the vacuum work function: for a generic case where $\mu = \Phi = 1$ eV, then $\tau_g = 0.65821$ fs. Compare this to the barrier width-dependent semiclassical time of Büttiker and Landauer [22] of $\tau_{sc} = L/\sqrt{2\Phi/m} = 1.6860$ fs for $L = 1$ nm, which has a very different nature. For the Hartman effect, Winful [23, 24] demonstrated that τ_g was the sum of a dwell τ_d and self-interference τ_i time.

A rectangular barrier is unlike a field emission barrier, for which the simplest representation is the triangular barrier of Fowler and Nordheim [25]. The delay time is therefore developed as follows. First, as per Winful, attention is explicitly restricted to energy eigenstates $\psi_k(x)$ (not wave packets). Second, the analysis of Winful is recast using the Gamow factor $\theta(k)$ to allow generalization. Third, the barrier is then taken to be the triangular barrier used by Fowler and Nordheim to develop their theory describing electron emission from a metal under high fields [25, 26]. Evaluations of the dwell τ_d and self-interference τ_i times for the field emission barrier are then developed and analyzed. Finally, the rectangular and triangular barriers shall be compared to two well-known barriers: the Schottky-Nordheim (SN) barrier (describing field emission from metals [25] and semiconductors [27]), and the Eckart barrier (an asymmetric barrier that allows an exact evaluation of $t(k)$ and $r(k)$).

3.1 Conventional Hartman Effect

The independence of τ_g on the width L of the rectangular barrier as L increases is termed the "Hartman effect". The rectangular barrier is given by

$$V_{rec}(x) = V_o\Theta(x)\Theta(L-x) \equiv \frac{\hbar^2 k_v^2}{2m}\Theta(x)\Theta(L-x) \tag{1}$$

where $\Theta(x)$ is the Heaviside step function, $V_o = \mu + \Phi \equiv \hbar^2 k_v^2/2m$ is the barrier height, and L is the barrier width. Winful [23, 24] demonstrates that τ_g is the sum of a dwell time τ_d and a self-interference time τ_i, respectively, given as

$$\tau_d(k) \equiv \left(\frac{m}{\hbar k}\right)\int_0^{L(k)} |\psi_k(x)|^2\, dx \tag{2}$$

$$\tau_i(k) \equiv -\frac{\hbar}{k}\Im[r(k)]\left(\frac{dk}{dE}\right) \tag{3}$$

$$\tau_g(k) \equiv \tau_d(k) + \tau_i(k) \tag{4}$$

where $\psi_k(x<0) = e^{ikx} + r(k)e^{-ikx}$ and $\psi_k(x>L) = t(k)e^{ikx}$, $\Im[r(k)]$ is the imaginary part of $r(k)$, $L(k)$ is the separation between where the wave function enters and emerges from a general barrier, $dk/dE = m/\hbar^2 k$, and $\hbar k$ is the momentum of the eigenstate. The transmission and reflection coefficients, $t(k)$ and $r(k)$, respectively, for $V_{rec}(x)$ for $k > k_v$ are [26]

$$\begin{aligned} t_{rec}(k) &= \frac{2k\kappa e^{-ikL}}{2k\kappa\cos(L\kappa) - i(k^2+\kappa^2)\sin(L\kappa)} \\ r_{rec}(k) &= \frac{-i(k^2-\kappa^2)\sin(L\kappa)}{2k\kappa\cos(L\kappa) - i(k^2+\kappa^2)\sin(L\kappa)} \end{aligned} \tag{5}$$

where $\kappa(k) \equiv |k_v^2 - k^2|^{1/2}$ so that κ is chosen to *always* be real and positive. The transmission probability is then $D_{rec}(k) = |t_{rec}(k)|^2$. For $k < k_v$ then $\kappa \to i\kappa$, causing the trigonometric terms to become their hyperbolic counterparts.

In the shape factor approach to tunneling [12, 13], the Gamow factor for $V_{rec}(x)$ is given by $\theta(k) \equiv 2\sigma\kappa(k)L$, where the tunneling width L is constant and the shape factor $\sigma = 1$ [13]. It is found for $k < k_v$

$$\Im[r(k)] = -\frac{2k\kappa k_v^2 \sinh\theta}{k_v^4[\cosh\theta - 1] + 2(2k\kappa)^2} \tag{6}$$

and therefore

$$\frac{\tau_i(k)}{\tau_o} = \left(\frac{\kappa k_v^4}{k}\right)\frac{\sinh\theta}{k_v^4(\cosh\theta - 1) + 2(2k\kappa)^2} \tag{7}$$

where $\tau_o = \hbar/V_o$. $\tau_d(k)$ requires the coefficients of the wave function inside the barrier, where $\psi_k(x) = a(k)e^{-\kappa x} + b(k)e^{\kappa x}$. They are solutions to

$$\begin{pmatrix} a(k) \\ b(k) \end{pmatrix} = \frac{1}{2\kappa}\begin{bmatrix} \kappa - ik & \kappa + ik \\ \kappa + ik & \kappa - ik \end{bmatrix}\begin{pmatrix} 1 \\ r(k) \end{pmatrix} \tag{8}$$

Insertion of $\psi_k(0<x<L)$ into Eq. (2) and using $\int_0^L e^{\pm 2\kappa x}dx = \pm(L/2)(e^{\pm\theta} - 1)/\theta$ results in

$$\frac{\tau_d(k)}{\tau_o} = \left(\frac{kk_v^2}{\kappa}\right)\frac{k_v^2\sinh\theta - (k^2-\kappa^2)\theta}{k_v^4(\cosh\theta - 1) + 2(2k\kappa)^2} \tag{9}$$

The McColl-Hartman effect, conventionally taken as a wide barrier ($L \to \infty$) limit, is now seen to be better understood as the $\theta \to \infty$ limit because θ can be large even when κ is small. Therefore [6]

$$\tau_d(k) = \tau_o\frac{k}{\kappa}\tanh\theta; \quad \tau_i(k) = \tau_o\frac{\kappa}{k}\tanh\theta \tag{10}$$

sothat $\tau_g \to \tau_o k_v^2/k\kappa$ is then recovered when $\theta \gtrsim 4$.

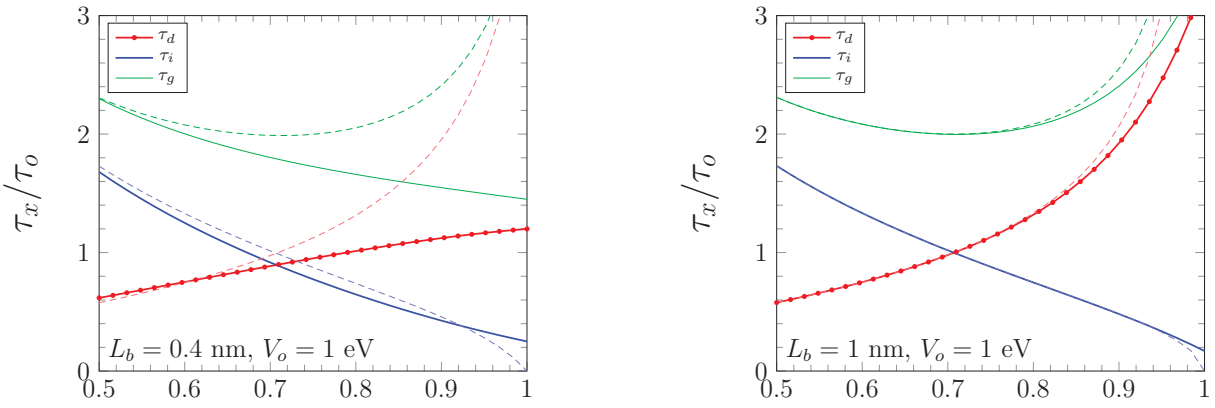

Figure 2: *Rectangular barrier dwell time τ_d (Eq. (7)), self-interference delay τ_i (Eq. (9)), and group delay τ_g as per Eq. (4) (solid lines) to the asymptotic large-θ form (Eq. (10), dashed lines) for increasing L.*

3.2 Departures from Hartman Effect for Rectangular Barrier

When $k = k_v$ the Gamow factor vanishes even though L is finite and large: when $k \to k_v$, then the small θ limit is required. It is found

$$\lim_{k\to k_v} \frac{\tau_d(k)}{\tau_o} = \frac{2Lk_v}{3}\left[\frac{(Lk_v)^2+3}{(Lk_v)^2+4}\right] \tag{11}$$

$$\lim_{k\to k_v} \frac{\tau_i(k)}{\tau_o} = \frac{Lk_v}{(Lk_v)^2+4} \tag{12}$$

In the large L limit when $k = k_v$, then

$$\lim_{L\to\infty} \frac{\tau_g(k_v)}{\tau_o} = \left(\frac{Lk_v}{3}\right)\frac{2(Lk_v)^2+9}{(Lk_v)^2+4} \to \frac{2}{3}Lk_v \tag{13}$$

as per Eq. (4) and therefore *is not independent of the barrier width* L when $k = k_v$. Thus, the independence of barrier width is a large θ limit rather than a large L limit, an important distinction because θ vanishes for $k = k_v$, where $\tau_g(k_v) = \tau_d(k_v)$ are finite. The behavior of τ_d, τ_i, and τ_g are shown in Figures 2 and 3 for increasing L.

3.3 Field Emission Modifications to Hartman Effect

Proceeding with the second step, the model of a rectangular barrier is undesirable in the consideration of field emission from a metal because, first (and practically), the tunneling process requires a large electric field to initiate the tunneling and cause it to dominate thermionic emission for which a rectangular barrier model is inadequate, and second (and aesthetically), when $k > k_v$ then the Airy function solutions to Schrödinger's equation behave such that $D_{fn}(k > k_v) \to 4k\kappa/(\kappa+k)^2$ when the applied field $\mathcal{E} \to 0$. The triangular barrier is given by

$$V(x>0) = V_o - Fx \equiv \frac{\hbar^2}{2m}\left[k_v^2 - fx\right] \tag{14}$$

and zero for $x < 0$, where $F = q|\mathcal{E}|$ contains the electric field $\mathcal{E}$, and q is the (positive) elementary charge unit, so that the charge of an electron is $-q$. The tunneling length factor L is now dependent upon F in Eq. (14), and therefore

$$L(k) = \frac{V_o - E}{F} = \frac{k_v^2 - k^2}{f} = \frac{\kappa(k)^2}{f} \tag{15}$$

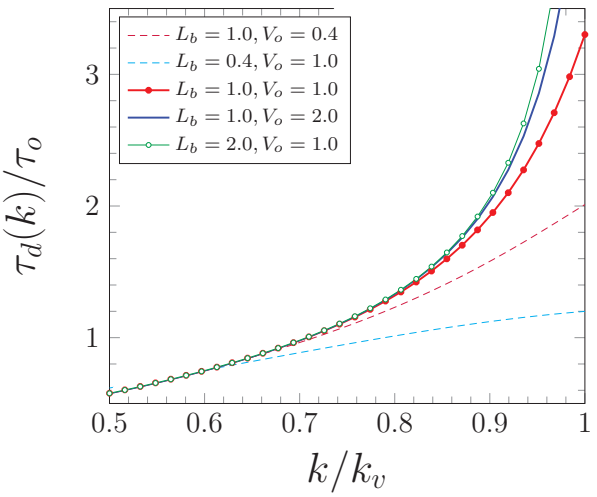

Figure 3: *The rectangular barrier $\tau_d(k)$ of Eq. (9) for various L_b and heights V_o, where $\theta \propto L_b\sqrt{V_o - E}$.*

for field emission conditions. For $x > 0$, $\psi_k(x) = t(k)\,[\mathrm{Ai}(w) - i\,\mathrm{Bi}(w)]$, where $w(x) = (k_v^2 - k^2 - fx)/f^{2/3}$. Using the asymptotic forms of the Airy functions, the transmission and reflection factors associated with the barrier of Eq. (14) lead to the self-interference time

$$\frac{\tau_i(k)}{\tau_o} = \frac{\pi f^{1/3} k_v^2\ \chi(\theta)}{k\left[\pi k^2 \Sigma(\theta) + \pi f^{2/3}\Sigma'(\theta) + 2f^{1/3}k\right]} \tag{16}$$

where for $k < k_v$, $\theta(k) = 4\kappa^3/3f = 2\sigma\kappa L$ for $\sigma = 2/3$ and $L(k) = \kappa^2/f$ [13], and

$$\begin{aligned} \Sigma(\theta) &= \mathrm{Ai}[w(0)]^2 + \mathrm{Bi}[w(0)]^2 \\ \Sigma'(\theta) &= \mathrm{Ai}'[w(0)]^2 + \mathrm{Bi}'[w(0)]^2 \\ \chi(\theta) &= \mathrm{Ai}[w(0)]\,\mathrm{Ai}'[w(0)] + \mathrm{Bi}[w(0)]\,\mathrm{Bi}'[w(0)] \end{aligned} \tag{17}$$

The large and small θ-limits have separate behavior. In the large θ limit, $\tau_i(k)$ becomes

$$\frac{\tau_i(k)}{\tau_o} \approx \frac{\kappa k_v^2}{k\,(k_v^2 + 2k\kappa e^{-\theta})} \tag{18}$$

and therefore approaches $\tau_i(k)/\tau_o \to \kappa/k$ as $\theta \to \infty$. In the $(k \to k_v)$ limit where $\theta \to 0$, $\tau_i(k)$ becomes

$$\begin{aligned} \frac{\tau_i(k_v)}{\tau_o} &= \frac{\pi f^{1/3} k_v\ \chi(0)}{\pi k_v^2 \Sigma(0) + \pi f^{2/3}\Sigma'(0) + 2f^{1/3}k_v} \\ &= \frac{\sqrt{3}\epsilon}{4\epsilon^2 + 6\epsilon + 3} \end{aligned} \tag{19}$$

where $\epsilon = f^{1/3}/\eta k_v$ where $\eta \equiv (4\pi/3)\,\mathrm{Bi}(0)^2 = 1.5839$. For finite F, $\tau_i(k_v)$ does not vanish. The behavior of $\tau_i(k)$ therefore mimics its analog for the rectangular barrier, where $f^{1/3}/\eta\sqrt{3}$ takes over the role of $1/L$. The dwell time $\tau_d(k)$ makes use of

$$\begin{aligned} |\psi_k(x)|^2 &= |t(k)|^2 \Sigma\left(\frac{4}{3}w(x)^{3/2}\right) \\ |t(k)|^2 &= \frac{4\pi k^2}{\pi k^2 \Sigma(\theta) + \pi f^{2/3}\Sigma'(\theta) + 2kf^{1/3}} \end{aligned} \tag{20}$$

where $\theta \equiv 4\kappa^3/3f$ as before, from which

$$\frac{\tau_d(k)}{\tau_o} = |t(k)|^2 \frac{k_v^2}{2kf^{1/3}} \int_0^\theta \frac{\Sigma(u)}{u^{1/3}} du \tag{21}$$

Again, the large and small θ-limits of $\tau_d(k)$ have separate behavior. In the large θ limit

$$\frac{\tau_d(k)}{\tau_o} \approx \frac{5k_v^2\kappa}{4\pi k f^{2/3}} |t(k)|^2 \left[1 + \delta(\theta)\right] \tag{22}$$

$$\delta(\theta) \equiv \frac{1}{15\theta^{1/3}} \int_0^\theta \frac{e^{-z} + 4e^z - 5}{z^{2/3}} dz \tag{23}$$

For large θ, $\delta \approx 4e^\theta/15\theta$ and $|t|^2 \approx 4\pi k^2\kappa e^{-\theta}/f^{1/3}k_v^2$, so

$$\frac{\tau_d(k)}{\tau_o} \approx \frac{k_v^2 f^{1/3}}{4\pi k\kappa^2} |t(k)|^2 e^\theta = \frac{k}{\kappa} \tag{24}$$

with the next order term going as $e^{-\theta}$, akin to Eq. (10). The large θ limit of τ_g is then the sum of Eqs. (19) and (22). In the small θ limit, the integrand in Eq. (21) may use a polynomial expansion for small argument of $\Sigma(u)$ from Eq. (17) and then integrated analytically term by term. It is found

$$\frac{\tau_d(k_v)}{\tau_o} \to |t(k_v)|^2 \left(\frac{\eta(k_v\kappa)^2}{2\pi f}\right) \left[1 + \frac{\kappa^2}{\sqrt{3}\eta f^{2/3}}\right] \tag{25}$$

which vanishes as κ^2 as $k \to k_v$ (compare Eq. (11)). The behavior of $\tau_d(k)$ is therefore *in contrast to the behavior of its analog* for the rectangular barrier, where $\tau_d(k)$ remains finite as $k \to k_v$ for finite L. An evaluation of $\tau_i(k)$ and $\tau_d(k)$ is shown for several representative fields and barrier heights in Figure 4 where, again, τ_g would be found as per Eq. (4). The larger $\theta(E) \propto (V_o - E)^{3/2}/F$ is, the better the approximations are. Notably, if applied to a wave packet composed of many components, and when either L or $1/f$ is large, then the more energetic components will increasingly constitute the outgoing packet, and they will therefore be associated with the smallest $\theta(k)$ factors. Efforts to bypass such complications by making very wide wave packets with a very narrow momentum spreads entail complications for the simulation of tunneling that are difficult. The relation $\tau_d(k)$ and $\tau_i(k)$ to the WDF analysis of wave packets of our prior work shall be taken up separately.

3.4 Extension to More Complex Barriers

A visual comparison of Figures 2 and 4 demonstrates similarities in the large θ-limit, even though the underlying potential barriers represent extreme cases. Therefore, as the final step of the analysis, consider two more representative barriers. The Schottky Nordheim (SN) barrier [26] describes field emission from metals and semiconductors by including image charge effects; it possesses an analytic θ but requires numerical evaluation for $t(k)$ and $r(k)$. The Eckart barrier is an asymmetric barrier which enables analytic $t(k)$ and $r(k)$ but requires a numerical evaluation of θ. Both are treated in tandem with regards to θ and suggested to be compatible with Eq. (10) as was Eq. (24). A confirmation of this can be had using an exact Airy Transfer Matrix Approach to solve Schrödinger's Equation [13] so as to obtain $\psi_k(x)$ exactly, and shall be undertaken separately. Therefore, here, Gamow behavior with respect to the scale factor $\sigma \equiv \theta/2\kappa L$ is undertaken. In both cases, the expressions for the location x_o of the maximum of the barrier, $\kappa(E) \equiv \sqrt{2m|V(x_o) - E|}/\hbar$, and the zeros $x_\pm(E)$ defined such that $V(x_\pm) - E = 0$ can be analytically found. Lastly

$$\sigma(E) \equiv \int_{x_-}^{x_+} \left[\frac{V(x) - E}{V(x_o) - E}\right]^{1/2} \frac{dx}{x_+ - x_-} \tag{26}$$

defines the shape factor and is evaluated here numerically. The terms are accordingly given by

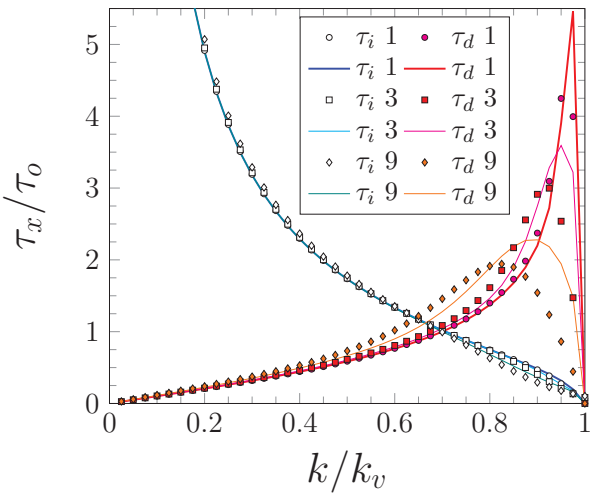

Figure 4: *Comparison of the exact* ($\circ, \square, \lozenge$) $\tau_i(k)$ *(Eq. (16)) and* ($\bullet, \blacksquare, \blacklozenge$) $\tau_d(k)$ *(Eq. (21)) to the approximations (lines) of Eq. (18) and Eq. (22), respectively. Legend is labeled by values of F [0.1 eV/nm]. $V_o = 1.25$ eV and $\tau_o = 0.52657$ fs. The subscript "x" on the τ_x axis label denotes either d or i.*

- Schottky-Nordheim:

$$\begin{aligned} V_{sn}(x) &= \mu + \Phi - Fx - Q/x \\ L(E) &= \left[\mu + \Phi - E)^2 - 4QF\right]^{1/2}/F \\ x_{\pm}(E) &= \left[\mu + \Phi - E \pm FL(E)\right]/2F \\ x_o &= \sqrt{Q/F} \end{aligned} \tag{27}$$

- Eckart:

$$\begin{aligned} V_e(x)/V_e(x_o) &= g(-x)(ag(x) - 1) \\ g(x) &= \left[\exp(x/b) + 1\right]^{-1} \\ x_{\pm}(E) &= b \ln\left[\frac{(a-1)(1 \pm \delta)}{a + 1 \mp (a-1)\delta}\right] \\ x_o &= b \ln\left[(a-1)/(a+1)\right] \end{aligned} \tag{28}$$

  where the parameters are chosen such that the Fermi level and work function are $\mu = \Phi = 2$ eV, the field is $F = 1$ eV/nm, the image charge term is $Q = 0.36$ eV-nm, $b = 1$ nm, $a = 1 + 2(\mu + \Phi) + 2\sqrt{(\mu + \Phi)(\mu + \Phi + 1)}$ is chosen so that the maximum of the barriers is the same, and δ is such that $E/V(x_o) = 1 - \delta^2$.

- Resonant: when a well structure is present within the barrier, due to charged defects or purposely engineered heterostructures, the transmission probability can approach unity for particular energy levels. The most common form is that of the resonant tunneling barrier, a two barrier structure with a rectangular well across which a bias can be imposed. A lorentzian factor is then included separate from the shape factor approach in the evaluation of $D(k)$.

The comparisons for SN and Eckart are shown in Figure 5. It is seen that the SN barrier stays closer to the triangular barrier (FN) case, but the Eckart potential moves closer to the parabolic case as E decreases. Interestingly, for energies closer to the barrier maximum, both SN and Eckart result in σ values that are reasonably close. The consequences on θ and therefore τ_d are taken up separately.

The possibility of resonances motivates the development of numerical Airy transfer matrix approach (Airy-TMA) methods. Resonances occur when $D(k)$ is sharply peaked about discrete energy values: these

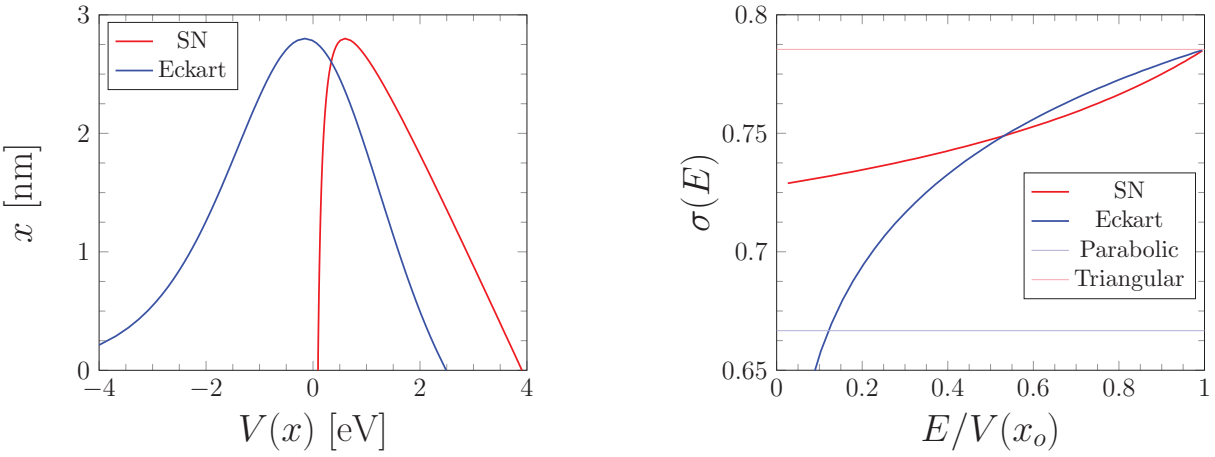

Figure 5: *(left) $V(x)$ for the SN and Eckart barriers for parameters in the text. (right) the resulting scale factor $\sigma(E)$ for each, where "Parabolic" and "Triangular" denote $\sigma(E) = (2/3, \pi/4)$ for the inverted parabolic and the triangular FN barriers, respectively, for which both are constant.*

values are associated with energy levels within a well region. The sensitivity of the resonance level on barrier and well properties is indicated by the behavior shown in Figure 6.

The susceptibility of thermal-field emission to structure within the barrier is dramatically revealed using Airy TMA on a triangular barrier with a small, almost inconsequential well, as shown in Figure 7. The development of an analytical thermal-field model to account for structure within $D(k)$ is complex, but clearly follows the general outlines of the simple triangular barrier FN model. When the barriers are rounded as a consequence of image charge modifications, as characteristic of a Schottky-Nordheim barrier on which the General Thermal Field (GTF) equation is based [8], it is seen that analytical methods based on a combination of shape factor methods and analytic transmission probability (Kemble) models can reasonably account for the variation, the development of which is ongoing. Finally, observe that metal-insulator-metal (MIM) barriers with image charge modifications [1] benefit analogously.

Thus, the self-interference τ_i and dwell τ_d as per Winful [23, 24] have been reevaluated for the rectangular (*aka* MIM) barrier and extended to the triangular (or field emission) barrier. Whereas conventionally the delay time is said to become independent of the width L of the barrier (the McColl-Hartman effect), it is seen that this conclusion *only* to conditions where the Gamow factor $\theta(k)$ is large (*e.g.*, where $k < \sqrt{k_v^2 - (2/L)^2}$): when θ is small, then τ_i and τ_d depend on L and in particular $\tau_d(k_v)$ grows with L. For the triangular or FN barrier characterized by the field term F, τ_d vanishes as κ^2, and therefore is in contrast to the rectangular barrier. The shape factor method readily gives the behaviors of the respective Gamow factors $\theta(E)$: work on that connection continues.

4 General Thermal-Field Emission and Generic Barriers

Field emission enables high brightness electron sources that are either applied to or under development for applications central to research, industrial applications and military technologies, such as particle accelerators and Free Electron Lasers, electron microscopes, vacuum nanoelectronics, and electron microscopy. In some applications, in particular High Power Microwave (HPM) devices and as charge neutralizers for thrusters used to maneuver satellites, a combination of temperature and curvature effects make the characterization of, and hence the modeling of, these sources both important and comparatively difficult: generally the electron emission equations are taken to be one of the canonical mechanisms, but the ignoring of temperature and curvature effects as generally done undercuts simulation accuracy and hence corrupts presumed beam characteristics: although not problematic for relatively blunt (or flat) emitters run very hot or at current

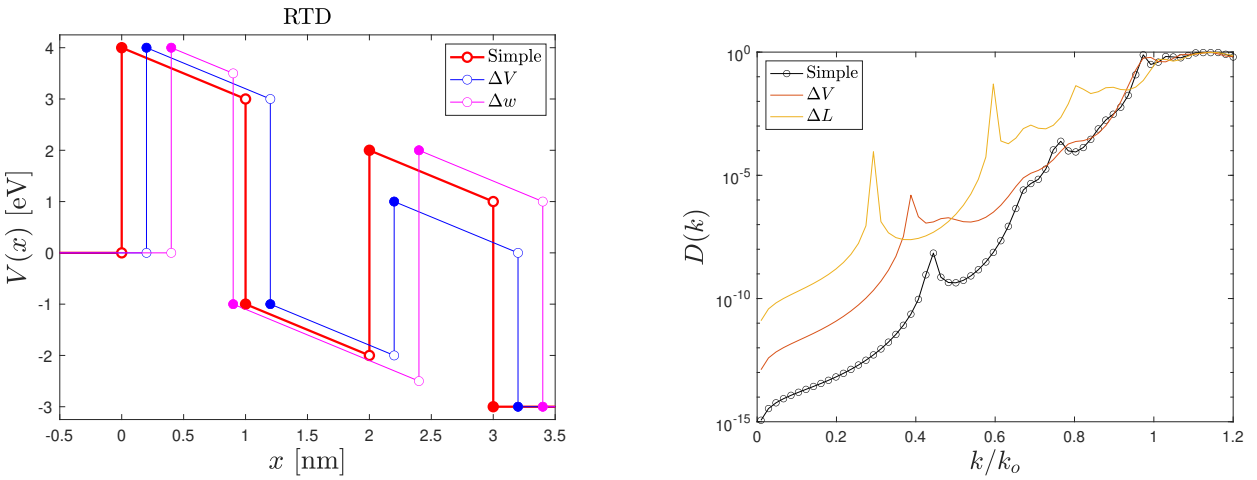

Figure 6: *(left) $V(x)$ for the RTD barrier and changes to the first barrier height (ΔV) or first barrier width (ΔL) for parameters given in the* `SETparam.m` *file of Appendix B.2. The modified barriers are offset from the primary (Simple) barrier to make the variations visible. The wave number k_o is related to the barrier height V_o by $V_o \equiv \hbar^2 k_o^2/2m$. Energy is $E(k) = \hbar^2 k^2/2m$. Airy TMA can return $D(k)$ in the thermal-field regime where $E > V_o$.*

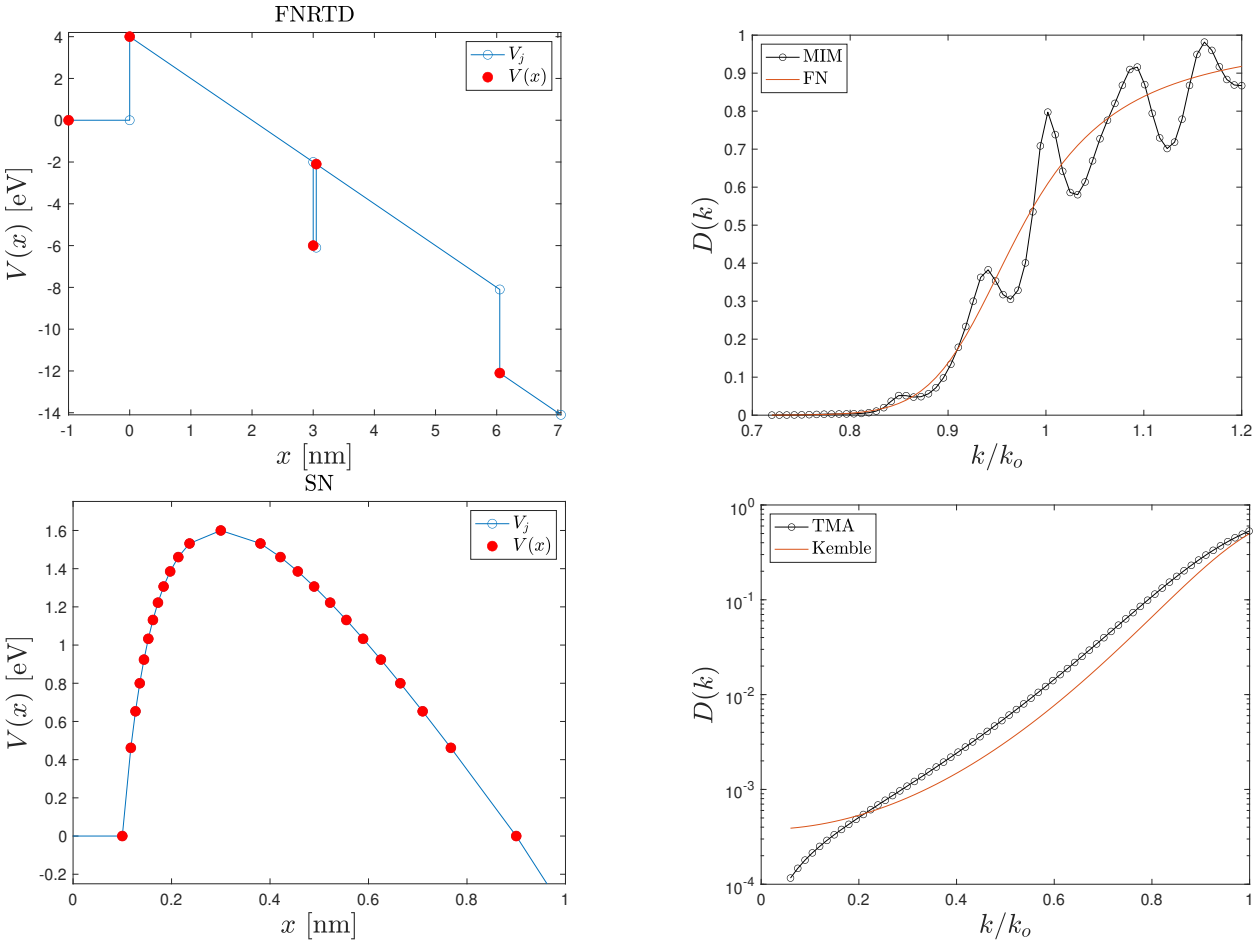

Figure 7: *(top left) $V(x)$ and (top right) $D(k)$ for the MIM barrier with a narrow well perturbation (ΔV) compared to the analytic triangular barrier FN (exact) solution. (bottom left) $V(x)$ and (bottom right) $D(k)$ for the Schottky-Nordheim barrier, which requires a fully numerical Airy TMA solution due to numerous barrier elements.*

levels where heat generation is not an issue, for high brightness sources in particular, where high current density and narrow angular spread of the beam are desired, multiple effects conspire to make their combined modeling difficult even if their underlying complications are individually well accounted for. A rapid and flexible methodology is desirable to correctly account for multiple complications in a manner that at best only mildly increases the numerical cost of execution, as needed for simulations with on the order of millions of surface elements contributing, or which utilize wire or nanogap emitters for which the emission barrier departs from the common Schottky-Nordheim barrier of standard field emission.

4.1 General Barriers

The shape factor method [28, 12, 8] gives an alternate method to the Schottky Nordheim functions for the treatment of the standard image charge barrier (alternately image-rounded barrier [29, 30] or Schottky Nordheim (SN) barrier [31]), but past developments using the shape factor approach have treated modifications to the barrier potential separately from the SN barrier. A standardized theory is developed that has as an asymptotic limit the SN barrier, but which will be clearly generalizable to more complicated barriers such as metal-insulator-metal (MIM), depletion/accumulation, and interface barriers. For MIM barriers in particular, a second image charge term must generally be included; if the insulator layer is sufficiently thin, then an infinite product of image charge terms must be included, but as shown before, the shape factor method can be adapted to deal efficiently with that configuration [1].

Let modifications to the SN barrier $V_o(x) = \mu + \Phi - Fx - Q/x$ be of the form of a polynomial $P_n(x)$ of degree n, or $P_n(x) = \sum_{j=2}^{n} C_j x^j$, so that

$$V_n(x) \equiv \mu + \Phi - Fx - \frac{Q}{x} + P_n(x) \tag{29}$$

where the conventions of prior efforts [26, 12] are used, specifically, units of [eV,fs,nm,q = 1] exclusively, q = unit (positive) charge, and the attachment of q to electric field $\mathcal{E}$ and potential φ to obtain factors of force $F \equiv q|\mathcal{E}|$ and energy $V = q\varphi$. Observe that although j could start at 0 so that $C_0 = \mu + \Phi$ and $C_1 = -F$, it is preferable not to do so and retain the special status of the up to linear terms explicitly, given the importance of the first two roots of the general barrier equation. The term containing Q is the image charge contribution, for which in conventional units, $Q = q^2/16\pi\varepsilon_0 = \alpha\hbar c/4$, or 0.36 eV-nm. Q can be trivially modified for semiconductors by the replacement $Q \to Q(K_s - 1)/(K_s + 1)$ where K_s is the dielectric constant [32, 33]. By virtue of the tunneling problem, restriction may be made to polynomials such that $V_n(x) - E$, where $E(k)$ is electron energy and k is wave number, has only real roots $x_j(E)$: imaginary roots are associated with conditions for which the tunneling probability $D(E) \approx 1/\{1 + \exp[\theta(E)]\}$ is driven to zero (infinitely thick barrier).

4.2 Semi-numerical Shape Factor Methods

The shape factor $\sigma_n(E)$ associated with $V_n(x)$ of Eq. (29) is explicitly defined by

$$\sigma_n(E) \equiv \int_{x_-}^{x_+} \left[\frac{V_n(x) - E}{V_n(x_o) - E}\right]^{1/2} \frac{dx}{x_+ - x_-} \tag{30}$$

where $(x_- < x_+)$ are the smallest two of the x_j roots defined by

$$V_n(x_j) - E \equiv 0; \quad \lim_{x \to x_o} \partial_x V_n(x) \equiv 0 \tag{31}$$

In terms of the shape factor, the Gamow factor $\theta_n(x)$ is then defined by

$$\begin{aligned} \theta_n(E) &\equiv 2\sigma_n(E)\kappa(E)L(E) \\ \frac{\hbar^2\kappa(E)^2}{2m} &\equiv V_n(x_o) - E \\ L(E) &\equiv x_+(E) - x_-(E) \end{aligned} \tag{32}$$

Define H as the height (in energy) of the barrier to the tunneling electron, or $H_n(E) \equiv \mu + \Phi - E$: by virtue of the definition of x_o, it is seen that x_o is dependent only upon F, Q, and P_j, but not on μ, Φ, and its dependence upon E is only through the dependence of the coefficients P_j in turn on E. By the definition of polynomials with real roots, it is seen immediately that

$$\sigma_n(E) = \int_{x_-}^{x_+} \left[\frac{x_o}{x} \prod_{j=1}^{n} \left(\frac{x - x_j}{x_o - x_j} \right) \right]^{1/2} \frac{dx}{x_+ - x_-} \tag{33}$$

The preferred form of the shape factor $\sigma_n(E)$ for further analysis is then Eq. (33). For numerical work, therefore, the task is to efficiently find the roots $x_j(E)$, the location of the turning points x_o and x_p, both defined as in Eq. (31) where the slope of the potential vanishes. The potential barrier is assumed to be such that $V_n(x > x_p) = V_n(x_p)$ (constant).

Space charge [11], doping [13, 1], and curvature near a nanoscale emission site [12] can often be well approximated by the $n = 2$ case, such that $P_2(x) \equiv \gamma x^2$: it is seen that $xV_2(x)$ is a cubic: consequently, this is referred to as the "quadratic barrier model." This is done for two reasons: first, the method to be developed below will be seen to be easily and straightforwardly extended to larger n, so that exposition is simplified by focusing on the cubic case; and second, the roots x_j for $j > 2$ will be large, making their contribution to Eq. (33) comparatively small. As a leading order approximation, therefore, quadratic $P_2(x) \equiv \gamma x^2$ are adequate for the leading order approximation modified at most by a small factor to be given below: it is suggested to be in general sufficient for numerical work.

4.3 Quadratic Barriers

Cubic equations with three real roots are historically known as *cases irreducibilis* (irreducible case) [34] because the straightforward methods for finding the roots initially developed involved imaginary numbers such that the roots were sums of complex conjugates: at the time (17^{th} century CE), imaginary numbers were perplexing. With some effort, the complex conjugates can be re-expressed in terms of trigonometric equations so that for the quadratic potential barrier, the equations for the roots x_j and maximum / minimum locations x_o and x_p are given by

$$\begin{aligned} \gamma x_j^3 - F x_j^2 + H x_j - Q &= 0 \\ 2\gamma x_o^3 - F x_o^2 + Q &= 0 \end{aligned} \tag{34}$$

where the root x_p follows the same equation as x_o but other than observing that x_o and x_p lie between the first and second pair of roots, respectively, x_p is not important in the present discussion. The roots of these equations satisfy the relations

$$\begin{aligned} F &= \gamma (x_1 + x_2 + x_3) \\ H &= \gamma (x_1 x_2 + x_1 x_3 + x_2 x_3) \\ Q &= \gamma (x_1 x_2 x_3) \end{aligned} \tag{35}$$

and are directly given by

$$x_j = \frac{F}{3\gamma} \left\{ 1 + 2\sqrt{1 - \delta^2} \cos \left[\frac{1}{3} (\varphi - 2\pi j) \right] \right\} \tag{36}$$

$$x_o = \frac{F}{6\gamma} \left[1 + 2 \cos \left(\chi - \frac{2\pi}{3} \right) \right] \tag{37}$$

$$x_p = \frac{F}{6\gamma} \left[1 + 2 \cos (\chi) \right] \tag{38}$$

where $x_2 < x_1 < x_3$: it is seen that for the parameterization of Eq. (36) that $x_- \Leftrightarrow x_2$ and $x_+ \Leftrightarrow x_1$. The angles are defined by

$$\cos \varphi \equiv \frac{8 - 12\delta + 3(y\delta)^2}{8[1 - \delta]^{3/2}}; \quad \cos(3\chi) \equiv 1 - \frac{3}{2}(y\delta)^2 \tag{39}$$

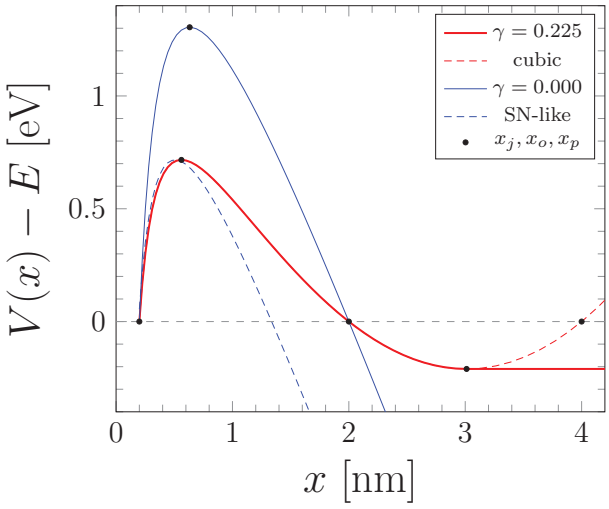

Figure 8: Quadratic (red, $\gamma > 0$) image charge barrier defined by the roots $x_1 = 2$, $x_2 = 0.2$ and $\gamma = 0.225$. For comparison, the $\gamma = 0$ standard image charge (SN) barrier with the same roots is also shown (blue), and an SN barrier having the same $[F, V(x_o)]$ labeled "SN-Like" (blue dashed). Black dots on horizontal axis (dashed grey) are roots x_j such that x_2 is the smallest and x_3 the largest. x_o and x_p on the lines mark turning points (where the slope is zero).

and the factors $\delta(E)$ and $y(E)$ are defined as

$$\delta \equiv \frac{3\gamma H}{F^2}; \quad y \equiv \frac{\sqrt{4QF}}{H} \tag{40}$$

Both δ and y can be defined in terms of the roots x_j using Eq. (35):

$$\delta = \frac{1}{6}\left[1 - \frac{\langle x_j^2 \rangle}{3\langle x_j \rangle^2}\right]; \quad y^2 = 2\left[1 - \frac{\langle x_j^{-2} \rangle}{3\langle x_j^{-1} \rangle^2}\right] \tag{41}$$

where $\langle \cdots \rangle$ denotes average. The factor $y(E)$ is the ratio of the Schottky barrier lowering factor $\sqrt{4QF}$ with the height H of the barrier above the electron energy E (Eq. (20) of Ref. [8]): for the special case of $E = \mu$, then $y(\mu)$ corresponds to the y parameter of Murphy and Good [35]. In computational parlance, Eq. (41) is vectorizable if the roots are specified: tables of lookup values, shown to significantly speed up execution when millions of emission elements are needed [36], can therefore be economically calculated. For example, generation of a parabolic image charge barrier using $\gamma = 0.225$ and $x_j = [2.0, 0.2, 4.0]$; also shown is the standard image charge barrier (blue) for the same roots x_1 and x_2 but for a field of $F = Q/x_1x_2$.

For $\gamma > 0$, then H is constrained: for energies $E < V(x_p)$, the transmission probability is driven to zero because the barrier has become infinitely thick. Eqs. (37) and (38) can then be used to bound E. For a given H, the transmission probability vanishes when γ exceeds a value γ_{max} for which $x_1 = x_3$, or, using Eq. (40), such that

$$\delta < \delta_{max} = \frac{12(1 - y^2)}{8 - 9y^2 + (4 - 3y^2)^{3/2}} \tag{42}$$

For purposes of analysis, though, specifying the third root x_j is not directly useful, because the specification of three roots chosen independently will alter the strength of the image charge factor Q, and that is unphysical. It is therefore preferable to eliminate the largest root x_3 in favor of Q such that $x_3 = Q/\gamma x_1 x_2$: therefore, σ will be constructed in terms of x_1, x_2, and Q for a given γ. The standard image charge barrier ($\gamma \to 0$) therefore corresponds to $x_3 \to \infty$. Ordered by size, the roots are $x_2 < x_1 < x_3$. Performing a

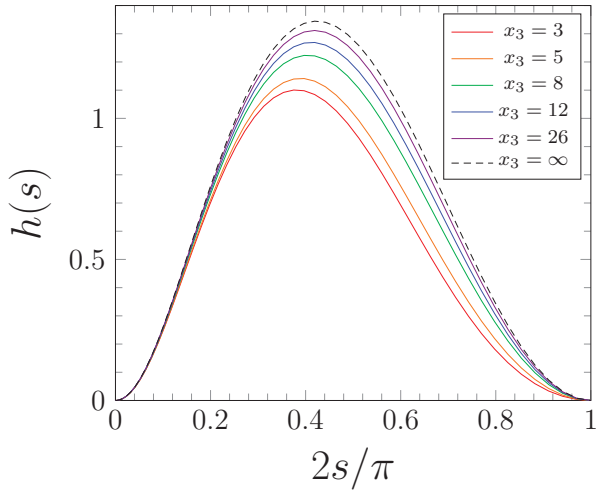

Figure 9: The integrand $h(s)$ for $Q = 0.36$ eV nm, $(x_1, x_2) = (2, 0.2)$ and various x_3 in nm.

change of variables such that $x \to x_2 + L\sin^2 s$ then (suppressing the $n = 2$ subscript on σ_n and $V_n(x)$)

$$\sigma(E) = \left(\frac{LQ}{4H_o x_1 x_2}\right)^{1/2} \int_0^{\pi/2} h(s)ds \tag{43}$$

$$h(s) = \left[\frac{1}{\sin^2 s + \varepsilon} - r\right]^{1/2} \sin^2(2s) \tag{44}$$

where $H_o = V(x_o) - E$ (the maximum of $V(x) - E$), $\varepsilon = x_2/L$, and $r \equiv L/x_3$. All of the roots and turning point locations have a dependence on E because they depend on H. Three limiting cases are analytic:

1. Triangular barrier: $K_s \to 1$ and $\gamma \to 0$, for which $x_2 \to 0$ and $\varepsilon \to 0$. Then $\int_0^{\pi/2} h(s)ds \to 4/3$, $\sqrt{LQ/4H_o x_1 x_2} \to 1/2$ and $\sigma \to 2/3$.
2. Parabolic barrier: $H_o \to 0$ (barrier becomes a parabola), $x_1 \approx x_o + L/2$ and $x_2 \approx x_o - L/2$ as $L \to 0$. $\int_0^{\pi/2} h(s)ds \to (\pi/4)\sqrt{L(x_3 - x_o)/x_o x_3}$ and $\sqrt{LQ/4H_o x_1 x_2} \to \sqrt{x_o x_3/[L(x_3 - x_o)]}$. Therefore, $\sigma \to \pi/4$.
3. Depletion barrier: $K_s \to 1$, $H_o = V(x_o) - V(x_p)$, then $x_3 = x_1$, $x_2 \to 0$, and $x_o \to 0$ (concave up parabolic barrier without image charge). $\sqrt{LQ/4H_o x_1 x_2} \to 1/2$ and so $\sigma \to 1/2$

The form of Eq. (43) is advantageous because the integral involving $h(s)$ varies over a narrow range, and the remaining terms are obtained through direct function evaluations. Because both $h(s)$ and its derivatives vanish at the integration boundaries, an Euler-MacLauren approximation makes Simpson's rule a good approximation [26]. Consequently, the summation

$$\int_0^{\pi/2} h(s)ds \approx \frac{\pi}{2(N+1)} \sum_{j=1}^{N} h(s_j) \tag{45}$$

where $s_j = j\pi/2(N+1)$, is numerically expedient because it can use vectorized algorithms, making the evaluation of σ for small N computationally rapid. The behavior of $h(s)$ for a constant $Q = 0.36$ eV nm and fixed roots $(x_1, x_2) = (3, 0.3)$ in nm, but varying x_3 which serves to change all (γ, F, H), is shown in Figure 9.

The evaluation of Eq. (43) exactly using Eq. (44) is compared to using Eq. (45) for various N in Figure 10 for three cases characterized by the conventional representation with $V_o = \mu + \Phi$ and $Q = (K_s - 1)Q_o/(K_s + 1)$

Table 1: Emission Barrier parameters in conventional representation in units of [eV] and [nm] for barrier height V_o [eV], field F [eV/nm], image charge factor Q [eV nm], and quadratic factor γ [eV nm^2], and the two turning points x_o [nm] and x_p [nm], for Figure 10.

Case	Symbol	V_o	F	Q	γ	x_o	x_p
1	□	2.0	0.25	0.0001	0.01	0.0200	12.5000
2	◇	2.0	3.00	0.3600	0.01	1.1396	14.9191
3	○	2.0	1.00	0.3600	0.10	0.6427	4.9258

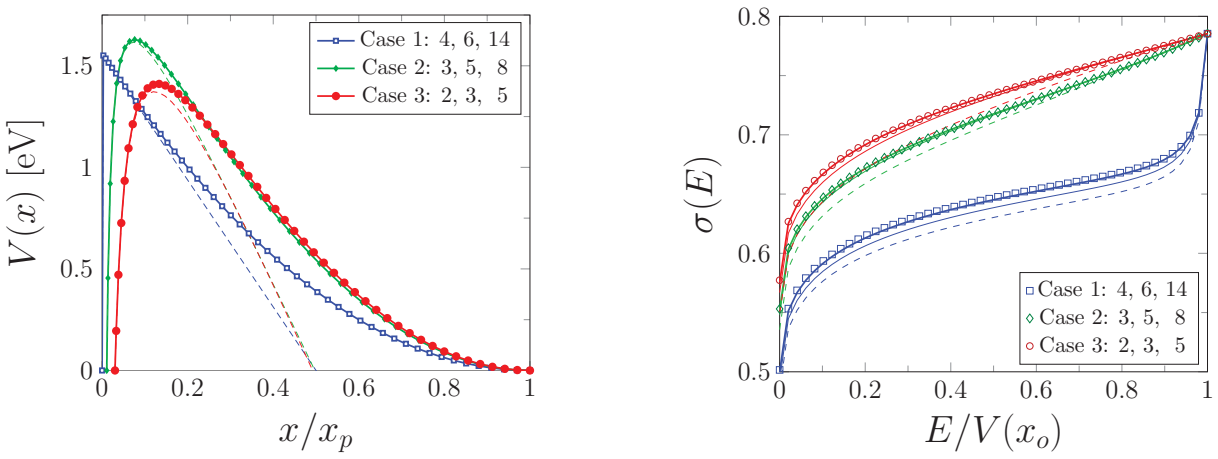

Figure 10: The integrand $h(s)$ for $Q = 0.36$ eV nm, $(x_1, x_2) = (2, 0.2)$ and various x_3 in nm.

to describe the barriers. The barriers are characterized by the four conventional parameters (V_o, F, Q, γ) and turning points (x_o, x_p) in Table 1. The associated barriers are shown in Figure 10(a), and the corresponding $\sigma(E)$ for $0 \le E \le V(x_o)$ in Figure 10(b). In the latter, symbols denote the exact evaluation using Eq. (43), and the lines (dashed, thin, thick) denote the N in increasing order in the approximation Eq. (45). Smooth, image charge rounded barriers allow for even small N resulting in good approximations, but even a difficult depletion barrier with only a minuscule image charge modification (Case 1) is well approximated for a manageable size of N. As a result, the Gamow $\theta(E)$ factors can be quickly and accurately evaluated without resorting to numerical integration. To evaluate current density using a GTF-based approach, $\theta(E)$ is best represented by a cubic in energy.

5 Thermal Effects Along a Fiber

5.1 Conical Model

In a prior study, the temperature variation along a cylindrical emitter was shown to increase. When conductors undergo constrictions, processes cause an increase in temperature [37, 38], therefore, as material from the cylindrical emitters ablates or is removed, it may be similarly expected that an associated temperature rise occurs. The temperature profile of a cone shaped emitter is therefore expected to depart from a cylindrical emitter along the length of the cone, although the underlying physics is similar to the cylindrical study [6]. When large currents were drawn from carbon fiber emitters [39], loss of material caused the wire diameter to thin and the apex to taper. To model the conductivity, treat the change in cross sectional area

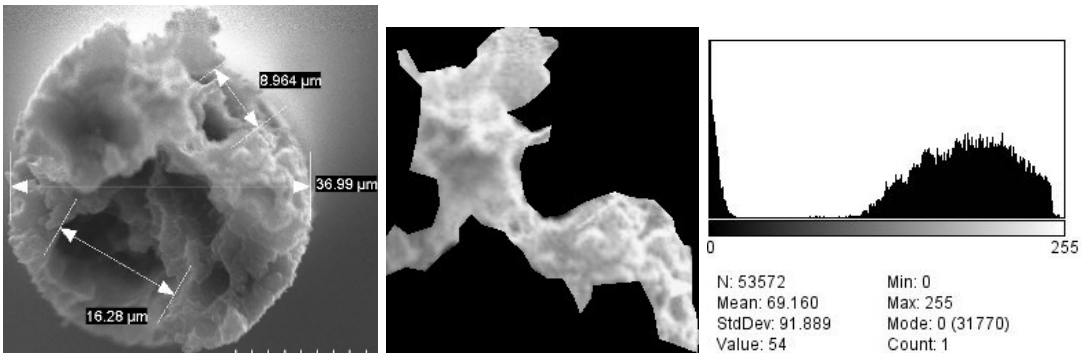

Figure 11: (*left*) Apex of carbon fiber (image courtesy of J. Connelly, AFRL); (*middle*) edited to exclude darkest regions for analysis by `imagej`; (*right*); resulting histogram.

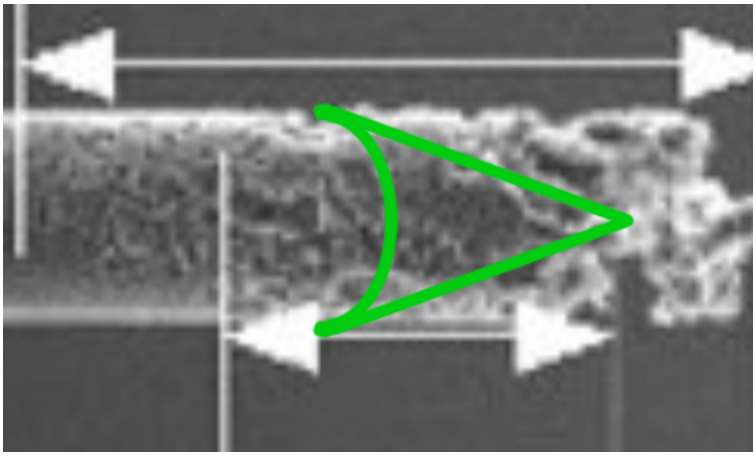

Figure 12: 20° Cone model: to estimate resistive properties of semi-conducting carbon, the cross sectional area along the length of damaged end of the wire was estimated based on the approximately 130 μm region shown in the figure (image courtesy of J. Connelly, AFRL).

as a gradually decreasing process.

The depth and extent of perforations on the carbon fiber were estimated based on the frequency of visible holes and color contrast of images from the prior study (see Figure 1, Ref. [6]). Using an image of the tip of a fiber shown in Figure 11, the variation in lightness of the pixels on a grayscale can be used to estimate the cross section such that a sum of the lightest pixels is proportional to the cross-sectional area of the fiber at that location. Estimates were also based on measurements of the depth and perforation frequency along the wire from associated images.

The cross sectional area estimates allowed for the modeling of damage as a cone with a half angle of approximately 20 degrees as shown in Figure 12. As the frequency and magnitude of the holes increased, much of the exterior was omitted due to the capacitor-like character of ledges and openings in the geometry. Omission of the exterior perforations allowed for the interpretation of the current carrying portions of the wire as a solid conical core.

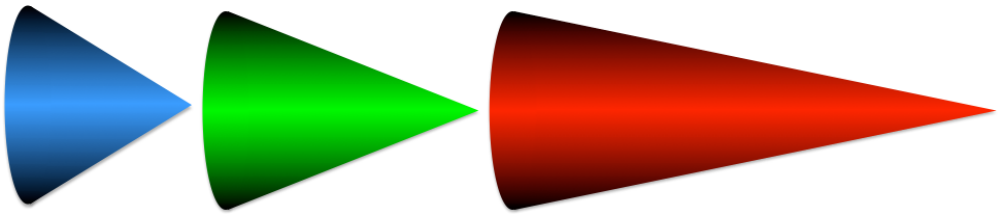

Figure 13: Model of Cones. Color of cone changes with cone angle (red is 10°, green is 20°, and blue is 30°) and corresponds lines in Figure 14.

Table 2: Parameters for carbon and copper-like. It is important to note that α is negative for Carbon due to its semiconducting properties. The emissivities are representative and affected by damages due to dynamic processes on the emitter apex.

Parameter	Symbol	Unit	Carbon	copper-like
Resistivity	ρ_o	$\Omega\ \mu$m	43.18	0.0172
ρ-Coefficient	α	10^{-3} /K	-0.166	3.93
Emissivity	ϵ	-	~ 1.0	~ 0.1

5.2 Temperature Model

Temperature profiles for two types of conical emitters were evaluated, one taken to be semiconducting carbon and the other to be metallic (copper-like) for comparison. Temperature along the length of the wire was evaluated assuming steady state current flow, so that no net heat was supplied to any element of the cone. For the region shown in Figure 11, Joule heating and radiative cooling processes both occur, suggesting that a segment of cone with (half) angle θ is governed by

$$\frac{\rho I^2}{A_c} dz = \epsilon \sigma_B \left(T^4 - T_o^4\right) dA_s \tag{46}$$

where z is the vertical distance along the cone (with $z = 0$ at the apex), $A_c = \pi r^2$ is the average cross-sectional area of a segment, $dA_s = 2\pi r$, and $dz/\cos\theta$ is the surface area contributing to radiative losses. Electrical parameters are ρ is the resistivity of the material, I is the current through the fiber and the same for each segment, ϵ is the emissivity, σ_B is the Stefan-Boltzmann constant, and T and T_o are the temperature of the segment and environmental background temperature, respectively. Manipulating gives

$$\rho I^2 = \epsilon \sigma_B (T^4 - T_o^4) \frac{2\pi^2 r^3}{\cos\theta} \tag{47}$$

A semiconductor model for resistivity as a function of temperature is taken to be

$$\rho = \rho_o[1 + \alpha(T - T_o)] \ , \tag{48}$$

which in combination with Eq. 47, gives:

$$\frac{\epsilon\, \sigma_B}{\rho_o I^2} \frac{2\pi^2 r^3}{\cos\theta} \left(T^4 - T_o^4\right) - \alpha \left(T - T_o\right) = 1 \ . \tag{49}$$

Temperature roots of this equation then determine the temperature profiles shown in Figure 14 and discussed below. Each radii value r, is associated with a distance $z = r/\tan\theta$ along the cone.

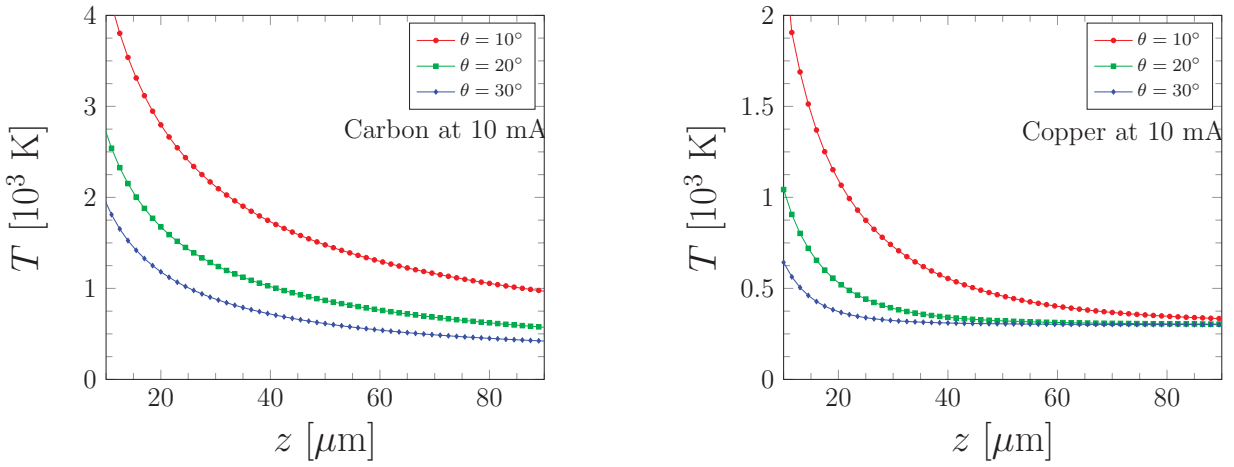

Figure 14: (*left*) Temperature profile of a conical carbon emitter conducting 10 mA current (steady state). Origin of z is at cone apex. θ is the half-angle of the cone. For comparison, a 20 μm radius carbon cylinder would reach 823 K. (*right* same, but for a conical copper-like emitter conducting 10 mA current For comparison, a 20 μm radius copper-like cylinder would remain at 300 K.

5.3 Simulation Results

The resistivity of a cone for three different half-angles was considered. The 20° angle is representative, but the 30° and 10° were investigated as well to assess sensitivity. As seen Figure 14, the temperature of a conical emitter steeply increases in proximity to the cone tip, as anticipated, for a steady state current taken to be 10 mA, a representative value for these fiber emitters. Variation of temperature strongly depends on the material parameters of Table 2, where "copper-like" is to mimic metal-like behavior, while acknowledging that the resistivity of physical metals [40] has a different behavior than semiconductors, so that the behavior is meant to be representative. For carbon, few configurations allow a temperature less than 1000 K, while for copper-like, temperatures exceeding 1000 K only occur within $5-20$ μm of the tip, due to the faster heat conduction associated with copper-like behavior. As the sublimation temperature of carbon is high most of the conical emitters resist sublimation down to radii below 20 μm. The melting temperature of a metal is much lower (*e.g.*, for copper, it is 1358 K). Nevertheless, at 10 μm radii, most of the fiber is expected to ablate material and become blunted owing to the high field enhancement of a fiber and the and high current density from the emission sites, as seen in Figure 11 where damage to the carbon fiber is evident.

At very high temperatures, thermal-field emission occurs, causing the presumed constancy of temperature along the cone to be progressively undermined, although field emission presumably dominates. To estimate this effect, the total current from differential surface elements must be estimated using the revised GTF equations accounting for the barrier modifications associated with curvature considered in Section 4.

6 Acknowledgements

We gratefully acknowledge discussions and interactions with

- Prof. D. Finkenstadt and M. K. Dhillon (US Naval Academy, Annapolis, MD)
- Dr. N. Riga (Directed Energy Directorate, Air Force Research Laboratory, Albuquerque, NM)
- Prof. J. L. Lebowitz (Departments of Mathematics and Physics, Rutgers University, NJ).

Appendicies

A Appendix: Schottky-Nordheim Theory

The standard Schottky-Nordheim barrier results are obtained in the limit $\gamma \to 0$, of the quadratic barrier of Sectionsec:quadbar, but the process requires care. The small γ limits of the roots (x_1, x_2) most easily handled by considering the combinations $x_1 \pm x_2$ and x_o. First,

$$L = x_1 - x_2 = \frac{2\sqrt{3}H}{F\delta}\sqrt{1-\delta}\ \sin(\varphi/3) \tag{50}$$

To leading order, $\varphi = \delta[(3/4)(1-y^2)]^{1/2}$, and so

$$L \approx \frac{H}{F}\sqrt{1-y^2}\sqrt{1-\delta} \tag{51}$$

Second,

$$\frac{x_1+x_2}{2} = \frac{H}{F\delta}\left[\frac{1-(1-\delta)\ \cos^2(\varphi/3)}{1+\sqrt{1-\delta}\ \cos(\varphi/3)}\right] \tag{52}$$

To leading order in φ again, or $\cos(\varphi/3) \to 1$,

$$\frac{x_1+x_2}{2} \approx \frac{H}{F}\left[\frac{1}{1+\sqrt{1-\delta}}\right] \tag{53}$$

Lastly, for x_o, use $\chi \approx 2\gamma\sqrt{3Q/F^3} = y\delta/\sqrt{3}$ to find in the limit of small γ

$$\begin{aligned} \lim_{\gamma\to 0} x_o &= \sqrt{\frac{Q}{F}} + \gamma\frac{Q}{F^2} \\ \lim_{\gamma\to 0} x_p &= \frac{F}{2\gamma} - 2\gamma\frac{Q}{F^2} \end{aligned} \tag{54}$$

As $\delta = 3\gamma H/F^2 \to 0$ in Eqs. (51), (53), and (54), the conventinonal Schottky-Nordheim results are recovered.

B Appendix: Numerical Evaluation of Transmission Probability

The transmission probability $D(k)$ may be evaluated using the highly accurate Airy Transfer Matrix Approach (Airy-TMA). The implementation here is using MATLAB, which now allows for function calls to Airy functions and their derivatives. For purposes of illustration, the computational algorithms to generate figures associated with Fowler Nordheim and Schottky-Nordheim barriers is shown. Methods to treat the Eckart barrier proceed analogously, but are not shown.

Airy-TMA methods are required when the potential at the rightmost boundary varies: conventional plane-wave TMA methods cannot be used accurately when the right contact is characterized by a non-zero field. Moreover, when potential variation exists, particularly for field emission conditions, the barrier can be accurately modeled using trapezoidal regions for which the Airy approach is ideal but the plane wave TMA would require a large number of rectangular barrier regions.

The plane wave TMA is simple to describe. At a transition (change in field) or discontinuity (change in potential) or both labeled by the position coordinate x_j, the wave function and its first derivative are matched at x_j. If k_j is the wave number to the right of x_j, then for vanishing f, the TMA matrices reduce to

$$\begin{aligned}
\mathbf{M}_j &= \frac{1}{\varphi_j^+ - \varphi_j^-}\begin{bmatrix} \varphi_j^+ \exp(\varphi_j^-) & -\varphi_j^- \exp(-\varphi_j^+) \\ -\varphi_j^- \exp(\varphi_j^+) & \varphi_j^+ \exp(-\varphi_j^-) \end{bmatrix} \\
\varphi_j^{\pm} &= i\,(k_j \pm k_{j-1})\,x_j \\
k_j &\equiv \left[\frac{2m}{\hbar^2}\,(E - V(x_j))\right]^{1/2}
\end{aligned} \tag{55}$$

The matrix elements are replaced by combinations of Airy functions when a field is present: the basis of the methodology is described separately [28, 26, 41]. The final matrix $\mathbf{M}_N$ for which $f > 0$ uses combinations of Airy functions that represents an outgoing wave for field emission conditions. The transmission probability is then

$$D(k) = \frac{f^{1/3}}{\pi k}\left|\left\{\prod_{j=1}^{N}\mathbf{M}_j\right\}_{1,1}\right|^{-2} \tag{56}$$

where $f = 2mF/\hbar^2$ and the subscript $(1,1)$ refers to the first row, first column entry of the resulting 2×2 matrix that results after the product of matrices is evaluated.

B.1 Primary Driver Routines

The generation of Potential barrier ($V(x)$) and TMA Transmission Probability ($D(k)$) are primarily executed for three representative conditions

- A barrier containing a well that creates resonances evocative of resonant tunneling structures `QBarrierRTD.m`
- A barrier that compares to the Triangular Barrier Fowler Nordheim model `QBarrierFN.m` so as to compare with analytical treatments
- A barrier that compares to the Schottky Nordheim barrier model `QBarrierSN.m`, where $D(k)$ can only be evaluated exactly using TMA methods, but can be compared to the Kemble approximation.

B.2 Constants and Parameters

Fundamental constants are loaded onto a Structure called `Pv` by `Fundamental.m` which can then be passed into function calls and subroutines. Use `SETparam.m` to load Structure parameters for the various simulations to be run.

```
function Pn = FUNdamental(P)
%% PACKAGE Afundamental.m
%-------------------------------------------------------------------------
% this function puts fundamental constants and terms needed
% into a structure for other program elements like Rhovector.m
% Included is a CLEAR statement to get rid of ones you don't use
% Modified last:  09-01-2021
% This version creates a structured form
%-------------------------------------------------------------------------

Pn = P;

% fundamental Constants in units of eV, fs, nm, q
    Pn.kb   = 1.0/11604.5181;   Pn.hbar  = 0.658211957;
    Pn.c     = 299.792458;      Pn.mo    = 5.68563010;
    Pn.afs  = 1.0/137.035999;   Pn.ao    = 0.0529177210;
% end fundamental constants
Pn.Qo = Pn.afs*Pn.hbar*Pn.c/4;
```

```
%% Subroutine SETparam
%  All units in eV, fs, nm, q=1
%  Default parameters for Fowler Nordheim and Eckart Potentials

Pv = struct;
Pv = FUNdamental(Pv);

Pv.Vo       = 4;
Pv.Field    = 4;
Pv.chem     = 2;
Pv.Phi      = Pv.Vo - Pv.chem;
Pv.re       = 1;

Pv.kmax = 1.2*sqrt(2*Pv.re*Pv.mo*Pv.Vo)/Pv.hbar;
Pv.kmin = 0.10;
Pv.Nk   = 64;
Pv.k    = Pv.kmin + (Pv.kmax - Pv.kmin)*(0:Pv.Nk-1)' / (Pv.Nk-1);

%% RTD parameters

Prtd = Pv;
Prtd.F    = 1;
Prtd.Nb   = 2;
Prtd.Vw   = 0;
Prtd.L    = 1; Prtd.w    = 1;
Prtd.Field= 0; Prtd.gamma = 0;
Prtd.ko   = sqrt(2*Prtd.re*Prtd.mo*Prtd.Vo)/Prtd.hbar;

%% FN parameters
Psn = Pv;
Psn.Nx = 12; Psn.p = 0.5;
Psn.kmax = sqrt(2*Psn.re*Psn.mo*(Psn.Vo-sqrt(4*Psn.Qo*Psn.Field)))/Psn.hbar;
Psn.kmin = 0.10*sqrt(2*Psn.re*Psn.mo*(Psn.Vo-sqrt(4*Psn.Qo*Psn.Field)))/Psn.hbar;
Psn.k    = Psn.kmin + (Psn.kmax - Psn.kmin)*(0:Psn.Nk-1)' / (Psn.Nk-1);
Psn.ko   = sqrt(2*Prtd.re*Prtd.mo*(Psn.Vo-sqrt(4*Psn.Qo*Psn.Field)))/Prtd.hbar;
```

B.3 Functions

Multiple function routines are used and listed here. TMA needs `FUNzi.m`, `FUNsmatrix.m`. Barriers are made by `FUNVxrtd.m`, `FUNVxsn.m`, and `FUNzi.m`. Auxiliary routines for comparison to conventional approaches are given by `FUNDkFN.m` and `FUNDkSN.m`.

```
function Gi = FUNzi(n,c,z)
% Calculation of the Gi function as a product of Zi and exp()
% airy(K,Z) returns various Airy functions specified by K:
%     K:  0 - Ai(Z), 1 - Ai'(Z), 2 - Bi(Z), 3 - Bi'(Z)
% airy(K,Z,SCALE) returns a scaled airy(K,Z) specified by SCALE:
%         0 - (default) is that same as airy(K,Z)
%         1 - returns airy(K,Z) scaled by EXP(2/3.*Z.^(3/2)) for K = 0,1,
%             and scaled by EXP(-ABS(2/3.*REAL(Z.^(3/2)))) for K = 2,3.

switch c;
    case 1
        if z < 1.0;
            Gi = airy(2+n,z)*exp(-(2.0/3)*z^1.5);
        else
            Gi = airy(2+n,z,1);
        end
    case 1i
        Gi = ((airy(n,-z)-1i*airy(2+n,-z))*exp(-(2.0/3)*1i*(z^1.5)));
    case -1i
        Gi = ((airy(n,-z)+1i*airy(2+n,-z))*exp( (2.0/3)*1i*(z^1.5)));
    case -1
        if z < 1.0;
            Gi = airy(n,z)*exp( (2.0/3)*z^1.5);
        else
            Gi = airy(n,z,1);
        end
end
```

```
function SM = FUNsmatrix(v,vp,L,k,Pv)
% Calculation of the basic matrix for the Transfer Matrix Approach
% Nomenclature:
%   vo = [Vo,Fo,xo] = present site (j)
%   vp = prior site (j-1)
%   L  = distance to j+1 site (if 0, you are at boundary)
% This version:  09/02/2021

alf = 2*Pv.re*Pv.mo/Pv.hbar^2;

%% structure of [v]:  v = (Vo,F,del)
%    Vo  = barrier height
%    F   = field; s = sign(F) 1 if F>1, -1 if F<1 and 0 otherwise
%    c   = 1 or i
%    del = x(n) - x(n-1)
% Observe that

k2 = k^2;

ko2  = alf*v(1);
so = 0; if abs(v(2)) > 5e-3; so   = sign(v(2));end
delo = v(3);

kp2  = alf*vp(1);
sp = 0; if abs(vp(2)) > 5e-3; sp   = sign(vp(2));end
delp = vp(3);

%% Begin matrix solution
% airy(K,Z) returns various Airy functions specified by K:
```

```
%     K:  0 - Ai(Z), 1 - Ai'(Z), 2 - Bi(Z), 3 - Bi'(Z)
% airy(K,Z,SCALE) returns a scaled airy(K,Z) specified by SCALE:
%         0 - (default) is that same as airy(K,Z)
%         1 - returns airy(K,Z) scaled by EXP(2/3.*Z.^(3/2)) for K = 0,1,
%             and scaled by EXP(-ABS(2/3.*REAL(Z.^(3/2)))) for K = 2,3.
% The matrix component is SM = SL*SR
%     SR uses vo; SL uses vp

%% Construct the SR matrix
if so == 0;
    kappa = sqrt(k2-ko2);
    SR = [       exp(1i*kappa*delo),           exp(-1i*kappa*delo);...
        1i*kappa*exp(1i*kappa*delo), -1i*kappa*exp(-1i*kappa*delo)];
else
    fo   = alf*abs(v(2));
    co   = 1.0; if ko2 < k2; co = 1i; end;
    qo   = so*(fo^(1./3));
    zo   = abs(ko2 - k2)/fo^(2.0/3);
    Ro   = exp(-(4.0/3)*co*(zo^1.5));
    SR = [FUNzi(0,co,zo)   , Ro*FUNzi(0,-co,zo)   ;...
        qo*FUNzi(1,co,zo), qo*Ro*FUNzi(1,-co,zo)]*exp((2.0/3)*co*(zo^1.5));
    if fo > 0.0;
        nl = sign(ko2-k2);
        nr = -1;
        if L > 0;nr = sign(ko2-k2+so*fo*L);end  %in a segment
        if nl > 0;
            if nr < 0; SR = SR*[-1i, 1i; 1 1]; end % under to over
        else
            if nr > 0; SR = 0.5*SR*[1i, 1; -1i, 1]; end; % over to under
        end
    end
end

%% Construct the SL matrix
if sp == 0;
    kappa = sqrt(k2 - kp2);
    SL = [kappa*exp(-1i*kappa*delo), -1i*exp(-1i*kappa*delo);...
        kappa*exp( 1i*kappa*delo),  1i*exp( 1i*kappa*delo)]/(2*kappa);
else
    fp   = alf*abs(vp(2));
    cp   = 1.0;  if kp2 + fp*sp*(delo-delp) < k2; cp = 1i; end;
    qp   = sp*(fp^(1./3));
    zp   = abs(kp2 + fp*sp*(delo-delp) - k2)/fp^(2.0/3);
    Rp   = exp( (4.0/3)*cp*(zp^1.5));
    Cof = (2*pi/(cp*qp*(1.0 - 3*cp^2)));
    SL = Cof*[ qp*FUNzi(1,-cp,zp)  , -FUNzi(0,-cp,zp)  ;...
        -qp*Rp*FUNzi(1,cp,zp),  Rp*FUNzi(0,cp,zp)]*exp(-(2.0/3)*cp*(zp^1.5));
end

SM = SL*SR;
```

```
function v = FUNVxrtd(Pv)
% function v = FUNVxrtd(Vo,Vw,xw,xb,Nb,F,Field,g)

Vo = Pv.Vo; Vw = Pv.Vw; xw = Pv.L; xb = Pv.w;
Nb = Pv.Nb;
F = Pv.F; Field = Pv.Field; g = Pv.gamma;

Vxc  = @(x,F,g) - F*x + g*x.^2;

% The Unit Barrier
xo  = [ 0, xb, xb, xb + xw];
Vxo = [Vo, Vo, Vw, Vw];
Nx = length(xo);

% The array barrier
```

```
x = zeros(1,Nb*Nx+1); Vx = x;
for j = 0:Nb-1
    x( j*Nx+2:j*Nx + Nx + 1) =  j*(xb+xw) + xo;
    Vx(j*Nx+2:j*Nx + Nx + 1) = Vxo;
end
Vx = Vx + Vxc(x,F,g);
Vx(Nb*Nx+1) = Vx(Nb*Nx) - Field*(x(Nb*Nx+1) - x(Nb*Nx));

Nx = length(x);
v = zeros(Nx,3);
io = 0;
for j = 1: Nx-1;
    if x(j+1) > x(j);
        io = io + 1;
        v(io,3) = x(j);
        v(io,2) = (Vx(j+1) - Vx(j))/(x(j+1) - x(j));
        v(io,1) = Vx(j);
    end
end
v = [v(1:io,1), v(1:io,2), v(1:io,3)];
```

```
function [Mv,xm] = FUNvfx(v)
% Potential Barrier plotting
% This version:  09/01/21

N = length(v(:,1));
Mv = zeros(2*N+2,3);
x =  v(:,3)'; V = v(:,1)'; F = v(:,2)';

% x coordinate
Mv(1,1)         = x(1) - 1;
Mv(2:2:2*N+1,1) = x;
Mv(3:2:2*N+1,1) = x;
Mv(2*N+2,1)     = x(N) + 1;

% V(x) value
Mv(3:2:2*N+1,2) = V';
Mv(4:2:2*N+1,2) = (V(1:N-1) + F(1:N-1).*(x(2:N) - x(1:N-1)))';
Mv(2*N+2,2)     = V(N) + F(N)*1;
Mv(:,3) = Mv(:,2);
Mv(2:2:2*N+2,3) = NaN;

xm = [Mv(1,1), Mv(2*N+2,1), min(Mv(:,2)), 1.05*max(Mv(:,2))];
```

```
function v = FUNVxsn(Pv)

F = Pv.Field; Vo = Pv.Vo; Q = Pv.Qo;
N = Pv.Nx; p = Pv.p;

Vxc  = @(x,v,f,q) v - f*x - (q./x);
Vox = Vo - sqrt(4*Q*F);

xo = sqrt(Q/Vo); E = Vox*(((0:N-1)')/N).^p;

L = sqrt(max((Vo - E).^2 - 4*F*Q,0))/F;
xm = ((Vo-E)/(2*F)) - L/2; xp = ((Vo-E)/(2*F)) + L/2;
x = [xm;xo;xp]; Vx = Vo - F*x - Q./x;
[~,io] = sort(x); x = x(io); Vx = Vx(io);

Nx = length(x);
v = zeros(Nx,3); v(:,3) = x; v(:,1) = Vx;
v(:,2) = [(Vx(2:Nx) - Vx(1:Nx-1))./(x(2:Nx) - x(1:Nx-1));-F];

```

```
end
```

```
function Dk = FUNDktma(Pv)
%% Based on DEtmacalc.m:  evaluation of D(k) using TMA


alf = 2*Pv.re*Pv.mo/Pv.hbar^2;
Nk = Pv.Nk;
v = Pv.vfx;
k = Pv.k;

N = length(v(:,1));
xo = v(1,3);
Field = -v(N,2);

Dk = zeros(Nk,1);
for jk = 1:Nk;
    Sx = [1,0;0,1];
    for ix = N:-1:2;
        vp = v(ix-1,:);
        vo = v(ix,:);
        L = 0;
        if ix < N; L = v(ix+1,3) - v(ix,3);end;
        SM = FUNsmatrix(vo,vp,L,k(jk),Pv);
        Sx = SM*Sx;
    end
    vp = [0, 0, xo-1.0];
    vo = v(1,:);
    L = v(2,3) - v(1,3);
    SM = FUNsmatrix(vo,vp,L,k(jk),Pv);
    Sx = SM*Sx;
    switch Field
        case 0
            p = sqrt(k(jk).^2 - alf*v(N,1))/k(jk);
            Dk(jk) = p/(abs(Sx(1,1))^2);
        otherwise
            p = ((1.0/pi)*(alf*Field)^(1./3))/k(jk);
            Dk(jk) = p/abs(Sx(1,1))^2;
    end
end
```

```
function Dk = FUNDkFN(Pv)
%% Fowler Nordheim Transmission probability

ABx = @(x) airy(0,x).^2 + airy(2,x).^2;
ABp = @(x) airy(1,x).^2 + airy(3,x).^2;

k = Pv.k; Vo = Pv.Vo; F = Pv.Field;

E = ((Pv.hbar*k).^2)/(2*Pv.re*Pv.mo);
f = 2*Pv.re*Pv.mo*F/Pv.hbar^2;f1 = f^(1.0/3); f2 = f^(2.0/3);
ko = sqrt(2*Pv.re*Pv.mo*Vo)/Pv.hbar;
kx = sqrt(2*Pv.re*Pv.mo*E)/Pv.hbar;
if F > 1e-4
    wx = (ko^2 - kx.^2)/f2;
    Dk = 4*f1*kx./(pi*((kx.^2).*ABx( wx) + f2*ABp( wx)) + (2 * f1*kx));
else
    kp = sqrt(max(kx.^2 - ko^2,0));
    Dk = 4*kx.*kp./(kx + kp).^2;
end

end
```

```
function Dk = FUNDkSN(Pv)
%% Schottky Nordheim Transmission probability

F = Pv.Field; Vo = Pv.Vo; Q = Pv.Qo;
Nk = Pv.Nk;

fx  = @(x,v,f,q) sqrt(v - f*x - (q./x));

theta = zeros(Nk,1);
E = ((Pv.hbar*Pv.k).^2)/(2*Pv.re*Pv.mo);
L = sqrt(((Vo - E).^2 - 4*F*Q))/F;
xm = (abs(Vo-E)/(2*F)) - L/2; xp = (abs(Vo-E)/(2*F)) + L/2;

for j = 1:Nk
    theta(j) = integral(@(x)fx(x,abs(Vo-E(j)),F,Q),xm(j),xp(j));
end
theta = (2*sqrt(2*Pv.re*Pv.mo)/Pv.hbar)*theta;

Dk = 1.0./(1 + exp(theta));

end
```

B.4 Graphics

Two plotting routines for giving Potential barrier ($V(x)$) and TMA Transmission Probability ($D(k)$) figures.

```
%% Plotting package:  SUBVxplot

[Mv,xm]  = FUNvfx(vfx);

if exist('ifln','var')  == 1; else; ifln = 1;end
if exist('filn','var')  == 1; else; filn = 'TEMP';end

figure(ifln)
plot(Mv(:,1),Mv(:,2),'-o','MarkerSize', 8); hold on
plot(Mv(:,1),Mv(:,3),'r.','MarkerSize',30); hold off;
set(gca,'fontsize',14)
xlabel('$x$ [nm]' ,'FontSize',24,'Interpreter','latex');
ylabel('$V(x)$ [eV]','FontSize',24,'Interpreter','latex');
legend({'$V_j$','$V(x)$'},'FontSize',16,'Location','northeast','Interpreter','latex')
title(filn,'Interpreter','latex','FontSize',20);
axis([xm(1) xm(2) xm(3) xm(4)])
```

```
%% Plotting package:  SUBDkplot

if exist('ifln','var')  == 1; else; ifln = 1;end
if exist('filn','var')  == 1; else; filn = 'TEMP';end
if exist('iopt','var')  == 1; else; iopt = 0;end
if exist('ltx','var')   == 1; else; ltx = {'TMA'};end

n = size(yy,2);
figure(ifln)
if n == 1
    if iopt > 0; plot(xx,yy); else; semilogy(xx,yy,'-or'); end
else
    if iopt > 0; plot(xx,yy(:,1),'-ok',xx,yy(:,2:n)); else
        semilogy(xx,yy(:,1),'-ok',xx,yy(:,2:n)); end
end
set(gca,'fontsize',14)
xlabel('$k/k_o$','FontSize',24,'Interpreter','latex');
ylabel('$D(k)$', 'FontSize',24,'Interpreter','latex');
legend(ltx(1:n),'FontSize',16,'Interpreter','latex','Location','northwest')
```

Index

References

[1] K. L. Jensen, A. Shabaev, S. G. Lambrakos, D. Finkenstadt, N. A. Moody, A. J. Neukirch, S. Tretiak, D. A. Shiffler, and J. J. Petillo, "Analytic model of electron transport through and over non-linear barriers," *J. Appl. Phys.*, vol. 127, no. 23, p. 235301, 2020. [Online]. Available: http://dx.doi.org/10.1063/5.0009759

[2] J.-W. Han, J. S. Oh, and M. Meyyappan, "Vacuum nanoelectronics: Back to the future?—gate insulated nanoscale vacuum channel transistor," *Appl. Phys. Lett.*, vol. 100, no. 21, p. 213505, 2012. [Online]. Available: https://doi.org/10.1063/1.4717751

[3] J.-W. Han, D.-I. Moon, and M. Meyyappan, "Nanoscale vacuum channel transistor," *Nano letters*, vol. 17, no. 4, pp. 2146–2151, 2017. [Online]. Available: https://pubs.acs.org/doi/abs/10.1021/acs.nanolett.6b04363

[4] M. R. Bionta, F. Ritzkowsky, M. Turchetti, Y. Yang, D. Cattozzo Mor, W. P. Putnam, F. X. Kärtner, K. K. Berggren, and P. D. Keathley, "On-chip sampling of optical fields with attosecond resolution," *Nat. Photon.*, vol. 15, no. 6, pp. 456–460, 2021. [Online]. Available: https://doi.org/10.1038/s41566-021-00792-0

[5] T. Rybka, M. Ludwig, M. F. Schmalz, V. Knittel, D. Brida, and A. Leitenstorfer, "Sub-cycle optical phase control of nanotunnelling in the single-electron regime," *Nat. Photon.*, vol. 10, no. 10, pp. 667–670, 2016. [Online]. Available: https://doi.org/10.1038/nphoton.2016.174

[6] K. L. Jensen, J. M. Connelly, J. J. Petillo, J. R. Harris, S. Ovtchinnikov, A. J. Jensen, J. Burke, M. Cahay, J. Ludwick, G. Tripathi, J. Sanchez-Roddy, and D. Puentes, "Semi-analytic model of a carbon fiber thermal-field emitter," *J. Appl. Phys.*, vol. 129, no. 9, p. 095107, 2021. [Online]. Available: http://dx.doi.org/10.1063/5.0044800

[7] E. Johnson, "Physical limitations on frequency and power parameters of transistors," *1958 IRE International Convention Record*, vol. 13, pp. 27–34, 1965. [Online]. Available: http://dx.doi.org/10.1109/irecon.1965.1147520

[8] K. L. Jensen, "A reformulated general thermal-field emission equation," *J. Appl. Phys.*, vol. 126, no. 6, pp. 065 302 / 1–13, 2019. [Online]. Available: http://dx.doi.org/10.1063/1.5109676

[9] K. L. Jensen, M. McDonald, J. R. Harris, D. A. Shiffler, M. Cahay, and J. J. Petillo, "Analytic model of a compound thermal-field emitter and its performance," *J. Appl. Phys.*, vol. 126, no. 24, p. 245301, 2019. [Online]. Available: http://dx.doi.org/10.1063/1.5132561

[10] K. L. Jensen, J. J. Petillo, S. Ovtchinnikov, N. Panagos, Dimitrios, N. A. Moody, and S. G. Lambrakos, "Modeling emission lag after photoexcitation," *J. Appl. Phys.*, vol. 122, no. 16, p. 164501, 2017. [Online]. Available: https://doi.org/10.1063/1.5008366

[11] K. L. Jensen, D. A. Shiffler, I. M. Rittersdorf, J. L. Lebowitz, J. R. Harris, Y. Y. Lau, J. J. Petillo, W. Tang, and J. W. Luginsland, "Discrete space charge affected field emission: Flat and hemisphere emitters," *J. Appl. Phys.*, vol. 117, no. 19, pp. 194 902 / 1–17, 2015. [Online]. Available: http://scitation.aip.org/content/aip/journal/jap/117/19/10.1063/1.4921186

[12] K. L. Jensen, D. A. Shiffler, M. Peckerar, J. R. Harris, and J. J. Petillo, "Current from a nano-gap hyperbolic diode using shape-factors: Theory," *J. Appl. Phys.*, vol. 122, no. 6, p. 064501, 2017. [Online]. Available: https://doi.org/10.1063/1.4997457

[13] K. L. Jensen, D. Finkenstadt, D. A. Shiffler, A. Shabaev, S. G. Lambrakos, N. A. Moody, and J. J. Petillo, "Analytical models of transmission probabilities for electron sources," *J. Appl. Phys.*, vol. 123, no. 6, p. 065301, 2018. [Online]. Available: https://doi.org/10.1063/1.5018602

[14] K. L. Jensen, D. A. Shiffler, J. L. Lebowitz, M. Cahay, and J. J. Petillo, "Analytic wigner distribution function for tunneling and trajectory models," *J. Appl. Phys.*, vol. 125, no. 11, p. 114303, 2019. [Online]. Available: https://aip.scitation.org/doi/abs/10.1063/1.5086434

[15] K. L. Jensen, J. L. Lebowitz, J. M. Riga, D. A. Shiffler, and R. Seviour, "Wigner wave packets: Transmission, reflection, and tunneling," *Phys. Rev. B*, vol. 103, p. 155427, 2021. [Online]. Available: https://doi.org/10.1103/PhysRevB.103.155427

[16] K. L. Jensen, M. McDonald, O. Chubenko, J. R. Harris, D. A. Shiffler, N. A. Moody, J. J. Petillo, and A. J. Jensen, "Thermal-field and photoemission from meso- and micro-scale features: Effects of screening and roughness on characterization and simulation," *J. Appl. Phys.*, vol. 125, no. 23, pp. 234 303 / 1–25, 2019. [Online]. Available: https://doi.org/10.1063/1.5097149

[17] P. Zhang, S. Fairchild, T. Back, and Y. Luo, "Field emission from carbon nanotube fibers in varying anode-cathode gap with the consideration of contact resistance," *AIP Advances*, vol. 7, no. 12, p. 125203, 2017. [Online]. Available: https://aip.scitation.org/doi/full/10.1063/1.5008995

[18] Y. Zhou and P. Zhang, "Theory of field emission from dielectric coated surfaces," *Physical Review Research*, vol. 2, no. 4, p. 043439, 2020. [Online]. Available: http://dx.doi.org/10.1103/physrevresearch.2.043439

[19] P. Zhang, A. Valfells, L. K. Ang, J. W. Luginsland, and Y. Y. Lau, "100 years of the physics of diodes," *Applied Physics Reviews*, vol. 4, no. 1, p. 011304, 2017. [Online]. Available: https://doi.org/10.1063/1.4978231

[20] T. E. Hartman, "Tunneling of a wave packet," *J. Appl. Phys.*, vol. 33, no. 12, pp. 3427–3433, 1962. [Online]. Available: https://aip.scitation.org/doi/pdf/10.1063/1.1702424

[21] L. A. MacColl, "Note on the transmission and reflection of wave packets by potential barriers," *Phys. Rev.*, vol. 40, pp. 621–626, May 1932. [Online]. Available: https://link.aps.org/doi/10.1103/PhysRev.40.621

[22] M. Büttiker and R. Landauer, "Traversal time for tunneling," *Phys. Rev. Lett.*, vol. 49, no. 23, pp. 1739–1742, 1982. [Online]. Available: http://dx.doi.org/10.1103/physrevlett.49.1739

[23] H. G. Winful, "Delay time and the hartman effect in quantum tunneling." *Phys. Rev. Lett.*, vol. 91, no. 26 Pt 1, p. 260401, 2003. [Online]. Available: https://doi.org/10.1103/PhysRevLett.91.260401

[24] ——, "Tunneling time, the hartman effect, and superluminality: A proposed resolution of an old paradox," *Phys. Rep.*, vol. 436, no. 1-2, pp. 1–69, 2006. [Online]. Available: http://dx.doi.org/10.1016/j.physrep.2006.09.002

[25] R. H. Fowler and L. Nordheim, "Electron emission in intense electric fields," *Proc. R. Soc. A*, vol. 119, no. 781, pp. 173–181, 1928. [Online]. Available: http://dx.doi.org/10.1098/rspa.1928.0091

[26] K. L. Jensen, *Introduction to the Physics of Electron Emission.* Hoboken, New Jersey: John Wiley & Sons, Inc., 2017. [Online]. Available: 10.1002/9781119051794

[27] R. Stratton, "Field emission from semiconductors," *Proceedings of the Physical Society. Section B*, vol. 68, no. 10, pp. 746–757, 1955. [Online]. Available: https://dx.doi.org/10.1088/0370-1301/68/10/307

[28] K. L. Jensen, "A quantum dipole–modified work function for a simplified electron emission barrier," *J. Appl. Phys.*, vol. 111, pp. 054 916 / 1–10, 2012. [Online]. Available: https://dx.doi.org/10.1063/1.3692571

[29] ——, "Electron emission physics," in *Advances in Imaging and Electron Physics Vol 149*, P. Hawkes, Ed. San Diego, CA: Elsevier, 2007, pp. 1–338.

[30] R. G. Forbes, "Use of energy-space diagrams in free-electron models of field electron emission," *Surf. Interface Anal.*, vol. 36, no. 5-6, pp. 395–401, 2004. [Online]. Available: https://doi.org/10.1002/sia.1900

[31] R. G. Forbes and J. H. B. Deane, "Reformulation of the standard theory of fowler-nordheim tunnelling and cold field electron emission," *Proc. R. Soc. A*, vol. 463, no. 2087, pp. 2907–2927, 2007. [Online]. Available: https://doi.org/10.1098/rspa.2007.0030

[32] R. Stratton, "Theory of field emission from semiconductors," *Phys. Rev.*, vol. 125, no. 1, pp. 67–82, 1962. [Online]. Available: https://doi.org/10.1103/PhysRev.125.67

[33] K. L. Jensen, "Improved fowler-nordheim equation for field-emission from semiconductors," *J. Vac. Sci. Technol. B*, vol. 13, no. 2, pp. 516–521, 1995. [Online]. Available: https://dx.doi.org/10.1116/1.588345

[34] D. S. Richeson, *Tales of impossibility : the 2000-year quest to solve the mathematical problems of antiquity.* Princeton, NJ: Princeton University Press, 2019.

[35] E. L. Murphy and R. H. Good, "Thermionic emission, field emission, and the transition region," *Phys. Rev.*, vol. 102, no. 6, pp. 1464–1473, 1956. [Online]. Available: https://doi.org/10.1103/PhysRev.102.1464

[36] J. Ludwick, M. M. Cahay, N. Hernandez, J. O'mara, K. L. Jensen, J. H. Deane, R. G. Forbes, and T. C. Back, "A new multiscale approach to rapidly determine the local emission current density of nanoscale metallic field emitters," *Journal of Applied Physics*, p. (accepted), 2021.

[37] P. Zhang, Y. Y. Lau, and R. M. Gilgenbach, "Thin film contact resistance with dissimilar materials," *J. Appl. Phys.*, vol. 109, no. 12, 2011. [Online]. Available: http://dx.doi.org/10.1063/1.3596759

[38] P. Zhang, D. M. H. Hung, and Y. Y. Lau, "Current flow in a 3-terminal thin film contact with dissimilar materials and general geometric aspect ratios," *Journal of Physics D - Applied Physics*, vol. 46, no. 6, 2013. [Online]. Available: http://dx.doi.org/10.1088/0022-3727/46/6/065502

[39] J. M. Connelly, W. W. Tang, J. R. Harris, and K. L. Jensen, "Demonstration of 3-d-printed field-emission cathodes," *IEEE Trans. Plas. Sci.*, p. 4292, 2019. [Online]. Available: http://dx.doi.org/10.1109/tps.2019.2931819

[40] N. W. Ashcroft and N. D. Mermin, *Solid state physics.* New York: Holt, Rinehart and Winston, 1976.

[41] K. L. Jensen, D. Finkenstadt, A. Shabaev, S. G. Lambrakos, N. A. Moody, J. J. Petillo, H. Yamaguchi, and F. Liu, "A photoemission moments model using density functional and transfer matrix methods applied to coating layers on surfaces: Theory," *J. Appl. Phys.*, vol. 123, no. 4, p. 045301, 2018. [Online]. Available: https://doi.org/10.1063/1.5008600